Communications Biology

https://doi.org/10.1038/s42003-026-10259-z

Article in Press

Spatial transcriptomic profiling of developing mouse hearts reveals a spatially patterned signaling environment

Received: 19 December 2025

Accepted: 5 May 2026

Cite this article as: Hu, J., He, H., Xu, J. *et al.* Spatial transcriptomic profiling of developing mouse hearts reveals a spatially patterned signaling environment. *Commun Biol* (2026). https://doi.org/10.1038/s42003-026-10259-z

Junqi Hu, Haoting He, Juan Xu, William A. MacDonald, Yuanhang He, Tianhao Liu, Wei Chen & Guang Li

Spatial transcriptomic profiling of developing mouse hearts reveals a spatially patterned signaling environment

Junqi Hu[1,2,#], Haoting He[1,#], Juan Xu[1], William A. MacDonald[3], Yuanhang He[1,2], Tianhao Liu[2,4], Wei Chen[4], Guang Li[1,*]

[1]Department of Cell Biology, University of Pittsburgh School of Medicine, Pittsburgh, PA, USA

[2]Tsinghua University, Tsinghua medicine, School of Medicine, Beijing, China

[3]Health Sciences Sequencing Core, University of Pittsburgh School of Medicine, Pittsburgh, PA, USA

[4]Department of Pediatrics, University of Pittsburgh, Pittsburgh, PA, USA

Key words: Heart development, Spatial Transcriptomic, Niche, Visium, Slide-seq, Conduction cell, EPDC, ablation

# These authors contributed equally to the work

* Corresponding author: Guang Li: guangli@pitt.edu

Abstract:

Heart development involves dynamic signaling interactions between cells and their surrounding environment (niche). Single-cell mRNA sequencing (scRNA-seq) has been widely used to profile gene expression in individual cells, but it faces challenges in dissecting niche signals due to the need for cell dissociation. In contrast, spatial transcriptomics can preserve tissue structure and represents a potentially effective approach for this purpose. In this study, we used two spatial transcriptomics platforms, 10x Genomics Visium and Curio Slide-seq (Curio Seeker), to generate a spatial atlas of hearts at embryonic and neonatal stages. Using Visium data, we analyzed the spatial patterns of cell cycle phases, compact and trabecular myocardium signatures, and chamber-specific genes across developmental progression. We discovered that atrial cardiomyocytes exhibit a mature myocardium transcriptional signature. Additionally, we identified the spatial patterns of signaling activities at different stages. Using Slide-seq data, we identified cardiac conduction cells, including cardiac neurons, sinoatrial nodal cells, atrioventricular nodal cells, and Purkinje fiber cells, and further studied their niche signaling. Moreover, by combining lineage tracing and spatial transcriptomics, we identified four types of epicardial cell-derived cells (EPDCs) and analyzed their signaling interactions with niche cells. We then eliminated the EPDCs using a cell ablation system and observed reduced signaling in the ablated hearts through spatial transcriptomics analysis. In summary, we generated a spatial transcriptomic atlas for developing mouse hearts and identified niche signaling for cardiac conduction cells and EPDCs.

Introduction:

The mouse heart develops into a four-chambered structure around E9.5, starting to incorporate fibroblasts and vascular cells at approximately E12.5. Heart cells continue to divide throughout the remainder of the embryonic period[1-4]. After birth, these cells adapt to

environmental changes, transitioning from hypoxia to normoxia, and continue to grow mainly through cardiomyocyte hypertrophy[5]. During developmental progression, different cardiac cells interact to regulate cell lineage specification, proliferation, and apoptosis, leading to the heart's final shape and function[6,7].

The cardiac conduction system plays a crucial role in synchronizing cardiac cell contractions to facilitate efficient pumping. It mainly consists of sinoatrial node (SAN) cells, atrioventricular node (AVN) cells, His-bundle (HB) cells, and Purkinje fiber (PF) cells[8,9]. All these components develop from cardiomyocytes (CMs). Specifically, SAN cells are derived from the sinus horn myocardium and are located outside the right atrium (RA). AVN cells originate from the atrioventricular canal myocardium and are positioned between the atrial and ventricular chambers. PF cells develop from the trabecular myocardium and reside within the ventricular chambers, while HB cells are derived from the primary ring and connect the AVN and PF cells[8,10]. In addition to these specialized cardiac conduction cells, the heart contains an intrinsic cardiac nervous system (ICNS), which includes parasympathetic and sympathetic neurons, local afferent neurons, and local circuit neurons. The ICNS, derived from neural crest cells, plays an essential role in regulating heart rate, coronary circulation, and the activity of the conduction system[11].

The epicardium is a cell layer on the outer surface of heart chambers[12,13]. Ablation of epicardial cells or mutation of the epicardial gene *Wt1* has been associated with severe heart defects[14,15]. Epicardial cells are known to secrete chemokines, such as FGF, which regulate heart development[16]. Additionally, through lineage tracing analysis, epicardial cells have been found to contribute to multiple cardiac lineages, including fibroblasts and smooth muscle cells, collectively termed epicardial cell-derived cells (EPDCs)[12,13,16]. However, how EPDCs interact with surrounding cells along their migration pathway remains unclear.

ScRNA-seq has been extensively used to study organ development including heart[17]. This approach excels at dissecting cellular heterogeneity and identifying lineage regulators. However, it has a significant limitation in that the original spatial context is lost during sample preparation. Spatial transcriptomics (ST), an emerging technology, has been used in many tissues to complement scRNA-seq studies. ST approaches are generally divided into imaging-based and sequencing-based methods[18]. Imaging-based methods, such as MERFISH and Xenium, provide high anatomical resolution but can only profile a limited number of target genes. In contrast, sequencing-based methods, like 10x Visium and Curio Slide-seq, enable genome-wide gene expression profiling, albeit with slightly lower resolution compared to imaging-based approaches. Importantly, both Visium and Slide-seq have proven effective for studying tissue development[19,20]. The 10x Visium platform has a better gene recovery rate, while Curio Slide-seq offers higher spatial resolution, making them ideal for profiling tissues of different sizes at late and early stages, respectively.

ST platforms, such as Visium and MERFISH, have been used to study human developing hearts but are limited to a few stages[19,21], restricting their ability to capture dynamic molecular changes throughout development. In this study, we used Visium and Slide-seq to profile developing mouse hearts at different stages, creating a spatial transcriptomic atlas. Specifically, we profiled six early stages using Slide-seq and six stages from E11.5 to P4 using Visium. We analyzed the atlas data with a focus on the maturation status of atrial CMs and the niche signaling in cardiac conduction cells. Furthermore, using lineage tracing mice, cell ablation assays, and Slide-seq, we identified the niche signaling of EPDCs and examined signaling changes following EPDC elimination.

Results:

Generation of a spatial transcriptomic atlas using Visium and Slide-seq

To profile genome-wide transcriptional expression in developing hearts, we used two different ST methods. First, we used Slide-seq to profile hearts at six early developmental stages, including E10.5, E11.5, E12.5, E13.5, E14.5, and E15.5 (Fig. 1A). Additionally, we retrieved ST data for hearts at E8.5 and E9.5, which were also profiled with Slide-seq[22]. Slide-seq relies on oligo-coated beads and achieves close to single-cell resolution. Meanwhile, we used Visium to profile hearts at six developmental stages: E11.5, E14.5, E16.5, E17.5, P0, and P2 (Fig. 1A). Although Visium has relatively lower resolution than Slide-seq, it provides higher gene recovery rates. Furthermore, Visium preserves tissue images, allowing gene expression data to be overlaid with tissue architecture for precise localization. The gene expression libraries from both methods were sequenced and analyzed using established bioinformatic pipelines, including reads mapping, counting, and normalization. After filtering out low-quality beads/spots, we identified 10,000–30,000 unique molecular identifiers (UMIs) and 3,000–5,000 genes per spot in the Visium data (Supplementary Fig. 1). In contrast, we detected a wide range of UMIs and genes per spot in the Slide-seq data, ranging from a few hundred to around one thousand (Supplementary Fig. 2).

Since neither ST method produces single-cell gene expression per bead/spot, we deconvolved the data to determine cell compositions. For Slide-seq data at E8.5 and E9.5, we performed cell type deconvolution using stage-matched scRNA-seq data[23] to identify the spatial locations of five CM subtypes: atrial, left ventricle (LV), right ventricle (RV), atrioventricular canal (AVC), and outflow tract (OFT) CMs (Supplementary Fig. 3A). For the remaining spatial data, deconvolution was conducted based on a previously generated scRNA-seq dataset that included multiple embryonic and neonatal stages[24]. From the deconvolution results, we identified multiple cell types per bead in the Slide-seq data. By plotting primary cell types, we observed the anatomical locations of atrial CMs, ventricular CMs, epicardial cells (Epi), immune cells, endocardial endothelial cells (EndoEC), fibroblasts (Fb), vascular endothelial cells (Vas_EC), and red blood cells (Fig. 1B). Specifically, we found that atrial and ventricular CMs were localized to the atrial and ventricular chambers, respectively, across all stages. Additionally, EndoECs were located inside the chambers, while Fbs were primarily positioned in the atrioventricular regions (Fig. 1B). Notably, although we recovered a small number of Vas_ECs and fibroblasts in the primary cell types, they were predominant in secondary cell types (Supplementary Fig. 3B). This indicates that Fbs and Vas_ECs were often captured on the same beads as CMs, and their marker gene expression was masked by CM gene expression.

We also deconvolved the Visium data to identify cell types in each spot and visualized the proportions of each cell type at each stage using pie charts. Consistent with the Slide-seq results, we observed that spots in the atria had a high proportion of atrial CMs, while ventricular spots showed a high proportion of ventricular CMs. In addition, AVC spots contained a high proportion of Fbs, though Fbs and other cell types were also detected in the chambers (Fig. 1C). These findings indicate that both ST datasets accurately captured the expected cardiac cell types and correctly mapped their spatial locations.

Atrial CM exhibits a transcriptional profile indicative of later developmental stages

Using the ST data, we next examined cellular heterogeneity. First, we annotated cell cycle phases in the spatial data using a set of cell cycle genes, including 40 S-phase genes and

53 G2M-phase genes[25]. In parallel, we scored compact and trabecular myocardium identities using a set of 500 genes differentially expressed in the two types of CMs in the scRNA-seq data (Fig. 2A, Supplementary Dataset 1)[24]. Interestingly, we found that the spatial patterns from these two analyses were largely consistent. In the Slide-seq data, G1-phase cells were primarily located within the chambers, whereas G2M/S-phase cells were found along the chamber wall and septum. Consistently, the myocardium scores showed that the trabecular signature was mainly located inside the chambers, while the compact signature was present on the chamber wall and septum (Fig. 2B, C). This shared pattern was also observed in the Visium data (Fig. 2D, E), aligning with previous reports suggesting differential cell cycle states between compact and trabecular myocardium[26,27].

Additionally, in the Visium data, we observed G1-phase and trabecular signatures in the atria across all analyzed stages (Fig. 2D, E), suggesting that atrial cells exhibit a trabecular-like gene signature. To verify this, we analyzed the expression of the trabecular gene *Nppa*[28]. We found that it was highly expressed in the ventricular trabecular region at E11.5 and E12.5. By E14.5 and E16.5, *Nppa* was expressed in both the ventricular trabecular and atrial regions, becoming atrial-specific by E17.5 and P2 (Fig. 2F, Supplementary Fig. 4A, B). This shift in *Nppa* expression suggests that the atrial cells share gene expression characteristics with ventricular trabecular myocardium.

We then analyzed the spatial expression patterns of left atrial (LA) and right atrial (RA) gene signatures. Using the top 500 differentially expressed genes from LA and RA CMs in scRNA-seq data[24], we did not observe distinct chamber-specific enrichment. However, when reduced to the top 20 genes, we identified clear LA and RA gene signatures (Fig. 3A, Supplementary Dataset 2). Among these, some genes, such as Adamts8, showed minimal expression at E11.5 but began expressing specifically in the LA by E17.5. Similarly, Bmp10 was primarily expressed in trabecular myocardium at E11.5, becoming RA-specific by E17.5 (Fig. 3B, 3C), illustrating a pattern shift from trabecular to atrial specificity.

We also analyzed genes differentially expressed in atrial and ventricular CMs, identifying *Myh6* and *Myh7*. A high *Myh6* to *Myh7* expression ratio is a known marker of CM maturation in mouse hearts. Interestingly, we observed that *Myh7* was consistently expressed in ventricular CMs from E11.5 to P2, while Myh6 was specifically expressed in atrial CMs at early stages and did not appear in ventricular CMs until E17.5 (Fig. 3D). Quantifying the *Myh6* to *Myh7* expression ratio in atrial and ventricular CMs using scRNA-seq data, we found that atrial CMs had higher ratios than ventricular CMs during late embryonic and early neonatal stages (Fig. 3E). These results suggest that atrial CMs exhibit a transcriptional profile indicative of later developmental stages than ventricular CMs at the same time points.

Spatial analysis of PDGF and BMP signaling pathways during developmental progression

Using the multi-staged Visium data, we next analyzed the spatial patterns of signaling activities throughout development. We applied an unsupervised method called COMMOT[29], which identified interactions from numerous ligand-receptor pairs with the consideration of spatial relationship. When visualizing the total number of interactions, we observed that these were predominantly enriched in the atrioventricular canal (AVC) and inner chamber layers (Fig. 4A). Additionally, scRNA-seq data were used to examine interactions among various cardiac cell types. We found that the PDGF pathway, although involving ligands from diverse cell types, had receptors largely enriched in non-cardiomyocytes (non-CMs) such as Fbs and mural cells. Among the four PDGF ligand-receptor pairs, the PDGFA-PDGFRA interaction appeared to act primarily on Fbs (Fig. 4B-D).

We then mapped PDGF pathway activity and the PDGFA-PDGFRA interaction on the spatial data, revealing that their signals were primarily concentrated in the AVC, OFT, and their derived structures such as valves and the root of large vessels, with receiving cells in these areas and sending cells located in adjacent chamber areas (Fig. 4E, F). Given that Fbs are enriched in the regions, this spatial pattern of signaling is consistent with the scRNA-seq predictions. Additionally, we analyzed downstream genes in the PDGF pathway, including those regulated both positively and negatively by PDGF signaling. Consistent with PDGF activity, positively regulated genes were primarily expressed in the regions, whereas negatively regulated genes showed diverse expression patterns outside the regions (Fig. 4G). We further analyzed the expression pattern of Pdgfra and Pdgfa on the spatial datasets and observed Pdgfra was highly enriched in the predicted regions, while Pdgfa was broadly expressed in the chamber regions (Supplementary Fig. 5). Next, we performed IF staining for Pdgfra on E15.5 and E17.5 heart sections. We observed expression in several tissue structures, including the roots of the large vessels, the valves, and a portion of the tissue posterior to the atria. The expression pattern varied across sections, some of which were consistent with the spatial transcriptomic profiles at the corresponding developmental stages (Supplementary Fig. 6A, B). In addition, lineage-tracing results using Pdgfra-CreER;Rosa-mTmG mice further confirmed that Pdgfra-positive cells were primarily enriched in the valves and in a small part of the atrial region within the analyzed sections (Supplementary Fig. 6C). Moreover, we stained for downstream effectors of PDGF pathway, including phosphorylated STAT3 (pSTAT3) and phosphorylated ERK (pERK) in E12.5 heart sections. Because signaling patterns may vary across different sections, we examined multiple sections for each effector. At E12.5, we observed that pERK signals were enriched in the tissue posterior to the atria in one section, at the roots of the large vessels in two sections, and in the valves and part of the atrial tissue in the remaining three sections (Supplementary Fig. 7A). For pSTAT3, we similarly observed enrichment in the roots of the large vessels, the valves, and portions of the atrial tissue (Supplementary Fig. 7C). We also stained for pERK at E15.5 and again observed enrichment in the large vessels and parts of the atrial tissue (Supplementary Fig. 7B). Regarding the presence of pERK signals in the atria and in epicardial cells of the ventricle in certain sections, we believe this likely reflects pERK activation by other signaling pathways such as EGF-EGFR, which has been reported to activate pERK and plays an important role in heart development[30]. Next, to investigate the function of the PDGF signaling pathway, we isolated the signal-sending and signal-receiving cell populations by generating a mouse model. Specifically, we crossed Pdgfra-CreER mice with Rosa26-mTmG reporter mice and administered tamoxifen to pregnant females at embryonic days E9.5 and E10.5 (Supplementary Fig. 8A). Embryos were harvested at E14.5, and eGFP signal was predominantly observed in the AVC region. We then microdissected the AVC tissue and isolated the $eGFP^+$ Fbs, the signal-receiving cells, using FACS. In parallel, we dissected the surrounding tissue, which served as the source of signaling cells. The $eGFP^+$ cells were then cultured either alone or co-cultured with the surrounding cells placed in a transwell insert. Both culture conditions were treated with either DMSO or 1 μM CP-673451 (PDGFR inhibitor) to assess the role of this signaling pathway (Supplementary Fig. 8B). After three days of culture, cells were collected and stained for Mki67 to evaluate proliferation (Supplementary Fig. 8C). In the condition where fibroblasts were cultured alone, both DMSO- and PDGFRi-treated cells showed a similar proportion of proliferating (Mki67+) eGFP+ fibroblasts. In contrast, under co-culture conditions, PDGFR inhibitor-treated cells exhibited a significantly higher proportion of Mki67+ fibroblasts compared to DMSO-treated cells. These results suggest that PDGF signaling inhibits fibroblast proliferation in the AVC region (Supplementary Fig. 8D, Supplementary Dataset 12).

We also examined the spatial distribution of BMP signaling. ScRNA-seq data identified multiple ligand-receptor interactions in the BMP pathway, with the Bmp6_ACVR1_BMPR2 pair being predominant (Supplementary Fig. 9A-C). Spatial analysis further indicated that BMP pathway activity was enriched in both the AVC and internal chambers at early stages, later

shifting to inner chambers (Supplementary Fig. 10A). The Bmp6_ACVR1_BMPR2 interaction exhibited a similar spatial pattern (Supplementary Fig. 10B). Notably, unlike the PDGFA-PDGFRA interaction, the Bmp6_ACVR1_BMPR2 interaction had the ligand Bmp6 expressed in Epis and EndoECs, while the receptors were expressed across multiple cell types. We also identified downstream genes regulated by the Bmp6 pathway, with positively regulated genes showing expression patterns consistent with Bmp6_ACVR1_BMPR2 activity, while negatively regulated genes exhibited complementary patterns (Supplementary Fig. 10C). Moreover, BMP2 and BMP4 are known to be expressed in CMs within the AVC and outflow tract (OFT). We have analyzed their spatial pattern and found that both were primarily enriched at the atrioventricular valves and the roots of the large vessels (Supplementary Fig. 11), consistent with previous reports in the literature[31,32]. To further assess BMP pathway activity, we performed immunofluorescence staining for the downstream effector, phosphorylated SMAD1/5 (pSMAD1/5). We observed strong pSMAD1/5 accumulation in the AVC and at the roots of the large vessels (Supplementary Fig. 7D), further supporting the findings from the spatial transcriptomic analysis.

Additionally, we analyzed a publicly available human spatial transcriptomic dataset, with a specific focus on two embryonic developmental stages: post-conception week (pcw) 6.5 and pcw9 (Supplementary Fig. 12A, F)[19]. Following deconvolution analysis, we identified all major cardiac cell types and observed spatial patterns similar to those in mouse embryonic hearts. Specifically, we observed that atrial and ventricular CMs were localized to the atrial and ventricular regions, respectively. Fbs were enriched in the AVC region, and endothelial cells were predominantly located within the cardiac chambers (Supplementary Fig. 12B, G). Next, we examined the distribution of cell cycle phases and the localization of compact and trabecular CMs. Although regional variations in both cell cycle states and myocardial subtypes were observed, the overall anatomical pattern did not fully align with that of the mouse heart (Supplementary Fig. 12C, H). This discrepancy may be attributed to the use of gene sets originally derived from mouse studies for classification. Furthermore, we analyzed the expression patterns of NPPA, MYH6, and MYH7. Their spatial expression in human hearts closely mirrored that in mouse hearts, with NPPA expressed in both atrial and trabecular regions, MYH6 in the atria, and MYH7 in the ventricles (Supplementary Fig. 12D, I). Finally, we investigated the spatial distribution of ligand–receptor interactions. The total number of interactions was enriched in the AVC region, large vessels, and inner chambers. We further specifically examined the spatial patterns of the PDGF and BMP signaling pathways, including the PDGFA–PDGFRA, BMP6–BMPR1A–BMPR2, and BMP4–BMPR1A–BMPR2 interactions. All pathways, except for BMP6–BMPR1A–BMPR2 at pcw9, showed strong accumulation in the AVC region (Supplementary Fig. 12E, J). These findings highlight the high degree of conservation between human and mouse embryonic heart development as revealed by spatial transcriptomics.

Identification of the signaling communications between conduction cells and their niche cells

Through the analysis of scRNA-seq data from micro-dissected zones of the conduction system[33], we identified conduction cells and their signaling interactions with other cell types. We began with cells derived from the SAN region. Consistent with previous findings[33], we identified a cluster of SAN cells with high expression of SAN markers like Hcn4[34], a neuronal gene-expressing cluster, and several other cell types, including atrial CMs, Endo_ECs, Vas_ECs, Epis, white blood cells, smooth muscle cells/pericytes, and blood cells (Fig. 5A-C). We further

conducted differential gene expression analysis between SAN cells and neuronal cells. SAN cells exhibited high expression of many CM genes, along with a set of SAN-specific genes such as *Shox2*, *Smoc2*, and *Cacna2d2*[35-37]. In contrast, neuronal cells showed high expression of *Phox2b*[38], *Isl1*[39], and other neuron-specific genes (Supplementary Fig. 13A). Next, we analyzed ligand-receptor interactions among these cell types, focusing on SAN and neuronal cells. Notably, SAN and neuronal cells were exposed to a shared set of signals, including Ptn, Mdk, and Igf, originating from various cell types (Fig. 5D, E).

Next, we identified conduction cells within the spatial data to analyze their interactions with neighboring cells. To validate our approach, we first tested it by examining interactions between Vas_ECs or Endo_ECs and their surrounding cells. After plotting the expression of the pan-EC gene *Pecam1*, Vas_EC marker *Fabp4*, and Endo_EC marker *Npr3* on E14.5 Slide-seq data, we observed that Fabp4 was mainly enriched in the outer chamber regions, while *Npr3* was mostly expressed within chambers (Supplementary Fig. 14A), consistent with their Vas_EC and Endo_EC identities. Selecting these EC types based on marker expression, we then identified one layer of surrounding cells for each (Supplementary Fig. 14B, C) and analyzed ligand-receptor interactions, focusing on signals from surrounding cells to target ECs. We identified distinct interaction patterns, with VEGFC specifically interacting with Vas_ECs and VEGFB with Endo_ECs, in line with reported differential VEGF signaling responses between these cell types[40,41] (Supplementary Fig. 14D, E). This confirmed our workflow's effectiveness for subsequent signaling analyses.

Using the E14.5 Slide-seq spatial transcriptomic data, we identified a group of cells located at the top of the right atrium that expressed SAN genes, such as *Shox2* and *Hcn4*. Additionally, we found a cluster of neuronal cells expressing *Phox2b* and several other neuronal genes (Fig. 5F). Based on the expression of *Shox2*, *Smoc2*, and *Cacna2d2*, three key genes prominently expressed in the SAN cluster from the scRNA-seq data[33] (Supplementary Fig. 13B), we selected the SAN cells and designated them as the target cell cluster. Meanwhile, we identified the neuron cells based on the expression of *Phox2b* and *Isl1* (Supplementary Fig. 13C), which was further supported by the expression of additional neuronal markers, including *Stmn3*, *Nefm*, *Tlx2*, and *Stmn2*[42-44] (Supplementary Fig. 13D). Next, we delineated the layer of cells surrounding these SAN and neuronal cells (Supplementary Fig. 15A, C). We then analyzed the signaling interactions between the target cells and their neighboring cells, identifying a distinct set of interactions for each group (Supplementary Dataset 3, 4). Notably, the ligands *Ptn*, *Mdk*, and *Igf1* were prominent in the interactions of both cell groups (Supplementary Fig. 15B, D). Finally, we mapped the spatial distribution of these three ligands, observing high expression in both the SAN and cardiac neuron regions (Fig. 5G).

Subsequently, we analyzed the scRNA-seq data derived from the AVN region. We identified AVN cells based on the expression of AVN-specific genes *Cacna2d2* and *Cpne5*[33,45] (Supplementary Fig. 16A, B). We then examined the interactions between AVN cells and other cell types, focusing primarily on signals from neighboring cells to the AVN cells. Similar to SAN cells, we found *Ptn*, *Mdk*, and *Igf* as major interaction pathways, along with Wnt and BMP signaling (Supplementary Fig. 16C). Next, we plotted the expression of AVN genes in the E14.5 spatial transcriptomic data (Supplementary Fig. 16D). By filtering through the combined expression of *Slc22a1*, *Cacna2d2*, and *Sln*[33], we identified several atrioventricular region-specific target spots (Supplementary Fig. 16E, F). We selected these spots and identified their surrounding cells. Subsequently, we studied the interactions between these two groups of cells (Supplementary Fig. 16G). Interestingly, we did not observe enrichment of the *Mdk*, *Ptn*, or *Igf*

pathways among the top interactions. Instead, we observed the *Angptl2* pathway, which is also identified in the scRNA-seq data (Supplementary Fig. 16G, Supplementary Dataset 3, 4).

We also examined PF cells in scRNA-seq data, identifying PF cells by *Gja5* and *Cacna2d2* expression[33,46] (Fig. 5H, I). Next, we analyzed the spatial data at E14.5 and identified a group of PF cells based on the positive expression of *Gja5*, *Cacna2d2*, and *Myl2*, as well as the absence of *Myl7* expression (Fig. 5J). We then selected the surrounding cells and analyzed the signaling interactions between them. We identified a set of ligand-receptor interactions from various pathways, including FGF and TGFβ, from surrounding cells to PF cells (Fig. 5K, Supplementary Fig. 17A-C, Supplementary Dataset 3, 4). We further plotted the expression of Fgf1 and Tgfb1 and found that both were highly expressed inside the chambers, with expression patterns similar to the distribution of PF cells (Fig. 5L). Furthermore, we analyzed the signaling from PF cells to the surrounding cells and found that Wnt4 and Sfrp5 were shared between the two lists (Supplementary Fig. 17D, E). We then plotted the expression of these two ligands and observed that both were expressed inside the chambers (Supplementary Fig. 17F).

Moreover, we analyzed heart sections at E15.5 and identified AVN cells based on the expression of the same three genes including *Slc22a1*, *Cacna2d2*, and *Sln*. We also identified PF cells based on the expression of *Gja5*, *Cacna2d2*, and *Myl2*, along with the absence of *Myl7* expression (Supplementary Fig. 18A, 19A). We then selected their surrounding cells and computed ligand–receptor interactions. Analysis of the two E15.5 heart sections revealed several pathways that are shared with those identified in E14.5 spatial transcriptomic data and single-cell RNA-seq datasets, including *Mdk*, *Bmp2*, and *Igf1* pathways (Supplementary Fig. 18B, C; 19B, C). For signaling from surrounding cells to PF cells, we also found multiple interactions shared with those detected in E14.5 spatial sections, such as *Thbs4*, *Vwf*, and *Vegfa* signaling (Supplementary Fig. 18D, E; 19D, E; Fig. 5K).

Lastly, we analyzed the expression patterns of conduction cell markers in the E12.5 and E13.5 spatial data. We did not observe distinct SAN, neuron, or AVN spots. However, we identified a group of PF cells in the ventricles at both stages (Supplementary Fig. 20A, C). Using the same combination of marker genes as in E14.5, we selected the PF cells and their surrounding cells and further analyzed their signaling interactions (Supplementary Fig. 20B, D). We examined the signaling from PF cells to the surrounding cells and vice versa (Supplementary Dataset 3, 4). We found a few shared signals, such as *Tgfb1*, but most signals were distinct between the stages, indicating dynamic environmental changes for the PF cells during developmental progression (Supplementary Fig. 21).

Signaling analysis of the niche of epicardium derived cells

Using the spatial transcriptomic approach, we also analyzed the signaling environment of epicardium-derived cells. We bred *Wt1-CreER* mice with a reporter mouse line, *Rosa26-mTmG*. After treating the pregnant mice with tamoxifen at E10.5 and E11.5, we collected the embryonic hearts at E14.5 for spatial transcriptomic profiling (Fig. 6A). To confirm the efficiency of lineage labeling, we performed the same experiment and collected embryos at E12.5 for eGFP signal imaging. We observed that most of the eGFP signal was localized on the outer surface of the chambers, indicating that the epicardium was efficiently labeled. In addition to the epicardium, some eGFP-positive cells were also identified inside the chamber, likely derived from the epicardium over the two days of tamoxifen treatment (Fig. 6B). Next, we reanalyzed a published scRNA-seq dataset of EPDCs[47]. Consistent with previous reports[47], we identified four

EPDC populations: epicardial progenitor (Epi_progenitor), epithelial-to-mesenchymal transition (EMT) cell, mesothelial cell, and mesenchymal cell (Fig. 6C). Through differential expression analysis of these four cell types, we identified their specific marker genes. Notably, we found *Upk3b*, *Sox9*, *Mt2*, and *Ramp2* to be marker genes for epicardial progenitors, EMT cells, mesothelial cells, and mesenchymal cells, respectively (Fig. 6D).

Moreover, we examined the spatial transcriptomic data at E14.5. We identified *eGFP* transcripts in both sections and found that the first section had a significantly higher number of spots compared to the second section (Fig. 6E, Supplementary Fig. 22A, 23, 24A). Furthermore, we combined the *eGFP* transcripts with one of the four lineage marker genes to identify specific EPDC subpopulations. Given that only a small proportion of Epis were captured in the sections, we identified only a few *eGFP+; Upk3b+* spots (Fig. 6F, Supplementary Fig. 22B, 24A, B). In contrast, we identified more cells in the other three populations. Regarding anatomical patterns, we observed that the *eGFP+ Sox9+* cells were predominantly located in the atrioventricular canal region in both sections. The *eGFP+ Mt2+* cells were primarily found in the compact myocardium and ventricular septum regions, while the *eGFP+ Ramp2+* cells were mostly located in the trabecular myocardium and ventricular septum regions (Fig. 6F, Supplementary Fig. 24A, B).

Next, we selected the cells surrounding the target cells and analyzed the signaling interactions between them (Supplementary Dataset 5-8). We assumed that all signals surrounding the target cells could potentially have important functions, so we did not perform discriminatory tests to differentiate surrounding from non-surrounding cells. Instead, we aimed to identify all interactions, regardless of whether they were also expressed in other cardiac regions. We first focused on the signaling from surrounding cells to EPDCs. We identified a large number of signaling interactions for each population, with significant overlap between the two sections. Specifically, we identified 10 shared ligands from surrounding cells to the *eGFP+ Upk3b+* cells, including *Fgf12*, *Lamc1*, *Tgfb1*, *Tgfb2*, *Wif1*, *Ybx1*, *Ntn1*, *Cxcl12*, *Efnb2,* and *Efnb3*. Among these ligands, we selected *Efnb2* and *Lamc1* for validation by staining their expression alongside *eGFP* and *Upk3b*. We observed that both ligands were expressed adjacent to *eGFP*$^{+}$*/Upk3b*$^{+}$ cells (Supplementary Fig. 25A, B), supporting the potential interactions predicted by spatial transcriptomic analysis. Efnb2 is a membrane-tethered ligand that has been reported to regulate multiple processes in heart development, including valve formation[48]. This is consistent with its relatively high expression in the AVC/OFT region and supports the idea that it may regulate interactions between the *eGFP*$^{+}$*;Upk3b*$^{+}$ cells and their surrounding cells. Additionally, Lamc1 is a subunit of laminin, a crucial extracellular matrix protein. It has been shown to be essential for epicardial cell migration and cardiomyocyte differentiation[49,50], suggesting an important role in mediating interactions between epicardial cells and other cardiac cell types. Moreover, we identified 15 ligands interacting with the *eGFP+ Sox9+* cells, such as *Actr2, Anxa1, Bmp7, Arf6, Ccn1, Ccn2, Efnb2, Fgf9, Wnt11, Fgf2, Tgfb2, Tgfb3, Fyn, Flt4,* and *Vegfa.* For the *eGFP+ Mt2+* cells, we identified signals like *Ccn1, Igf2, Il4, Dhh, Flt4, Efnb1, Efnb2, Fgf1, Hbegf, Icam1, Cxcl12, and Fyn. For the eGFP+ Ramp2+* cells, we found *Bmp10, Bmp2, Bmp7, Ccl2, Ccn2, Fgf7, Il2, Wnt5a, Dcn, Cxcl12,* and *Edn1* (Fig. 6G, Supplementary Fig. 26A). The ligands were largely distinct for each EPDC population, suggesting they are exposed to different niche environments.

Lastly, we analyzed the signals from EPDCs to the surrounding cells (Supplementary Dataset 5-8). Interestingly, we identified fewer shared signals between the two E14.5 sections for each EPDC type. Specifically, we found only three ligands—*Wnt5a, Efna5*, and *Tln1*—for the *eGFP+ Upk3b+* cells; four ligands—*Lamc1, Sema6d, Lama4*, and *Lman1*—for the *eGFP+*

Sox9+ cells; three ligands—*ARF6, Gdf15*, and *Hspa8*—for the *eGFP*+ *Mt2*+ cells; and two ligands—*Jam3 and Lama4*—for the *eGFP*+ *Ramp2*+ cells (Supplementary Fig. 26B, C). These results suggest that the influence of different EPDC populations on neighboring cells appears to be highly dependent on spatial position.

Spatial analysis of the defects in epicardium-deficient hearts

To understand how EPDCs influence embryonic heart development, we employed a cell ablation strategy by breeding a *Wt1-CreER* mouse strain with a *Rosa26-DTA* mouse strain (Fig. 7A). We treated the pregnant mice with tamoxifen at E10.5 and harvested the embryos at E12.5. No significant differences were observed in the ablated mice compared to the control group. However, we found that the ablated hearts exhibited bifid apices and a more rounded shape than the control hearts, defects similar to those observed in Wt1 mutant hearts[14,24] (Fig. 7A).

Next, we profiled the ablated hearts at E12.5 using Slide-seq and compared them to the E12.5 CD1 spatial data. We first analyzed the control and ablated sections using the gene modules for compact and trabecular myocardium. We found that the mutant sections exhibited expanded trabecular regions in the chambers compared to the controls, with a noticeable expansion toward the ventricular septum (Fig. 7B). Given that epicardial progenitor and EMT cells are the major types of EPDCs identified in scRNA-seq analysis at this stage[47], we analyzed the location of EMT cells by plotting the expression of *Sox9*. We observed a significant reduction in *Sox9* signal in both ablated sections compared to the control section (Fig. 7C), suggesting efficient ablation of EPDCs in both embryos.

Given the similarity between the defects in epicardium ablated and *Wt1* mutant hearts, we analyzed the ligand-receptor interactions between Fbs and Ven_CMs using scRNA-seq data from Wt1 mutant and control hearts[24], identifying fibroblast signals that regulated differentially expressed genes in Ven_CMs. We found that signals such as Inhba potentially regulated a group of genes (Fig. 7D). Consistently, spatial sections showed reduced Inhba expression in the ablated heart sections compared to controls (Fig. 7E). Lastly, we observed a decrease in *Vim* expression in *Wt1* mutant Ven_CMs compared to controls in the scRNA-seq data (Supplementary Fig. 27A), which was confirmed in spatial sections showing reduced expression in the ablated hearts (Fig. 7F).

We further analyzed the signaling changes around CMs and ECs following EPDC ablation. Since trabecular myocardium expanded in the ablated hearts, we separated compact and trabecular CMs for analysis. Compact CMs were identified by the expression of *Hey2*, *Myl2*, and the absence of *Nppa*, while trabecular CMs were identified by the expression of *Nppa* and *Slit2*. For ECs, since Vas_EC had not developed at E12.5, we identified EndoECs based on the expression of *Pecam1* and *Npr3* (Supplementary Fig. 27B). We selected these three cell groups and their surrounding cells to analyze signaling communications. Interestingly, we found that the number of signals from surrounding cells to these groups was lower in the ablation hearts compared to controls (Supplementary Dataset 9-11), indicating a loss of signaling after EPDC ablation. For example, we observed a loss of Sema3d signaling around EndoECs (Fig. 7G). We then assessed *Sema3d* and *Npr3* expression in control and EPDC-ablated hearts at E12.5. Compared to controls, ablated hearts exhibited a clear reduction in *Sema3d* signal. Specifically, in control hearts, the signal on the heart surface was continuous, whereas in ablated hearts it was discontinuous. We also observed a reduction of the signal in the AVC region of ablated

hearts compared to controls (Fig. 7H, Supplementary Fig. 28). Further quantification of the *Sema3d* signal relative to DAPI-stained nuclei revealed a significant reduction in ablated hearts (Fig. 7I, Supplementary Dataset 12). These findings suggest that EPDCs contribute to heart development by signaling to support other cardiac cell types.

Discussion:

In this study, we used 10x Visium and Curio Slide-seq to generate a spatial atlas of developing hearts at embryonic and neonatal stages. We then employed the Visium data to analyze the spatial patterns of gene expression and signaling activities across these developmental stages. This represents a comprehensive cardiac spatial dataset and serves as a valuable resource for the field of heart development, supporting a variety of applications such as analyzing expression patterns of candidate genes and signaling pathways. Using the Slide-seq data, we investigated niche signaling in cardiac conduction cells and EPDCs, and further examined the signaling defects following EPDC ablation. This represents a study of signaling exchanges between EPDCs and their surrounding cells under both normal and defective conditions. Overall, we believe this study provides a systematic understanding of the signaling microenvironments involved in heart development.

The Visium data provides a high number of genes with lower spatial resolution, while the Slide-seq data captures fewer genes with higher spatial resolution. Visium requires lower sequencing depth and can be effectively analyzed using resource-efficient bioinformatic algorithms like Cell2Location[51]. In contrast, Slide-seq demands deeper sequencing and more analytical resources. As a result, the Visium system is suitable for profiling large tissues, such as neonatal and adult mouse hearts, while Slide-seq is better suited for analyzing smaller tissue samples, such as early-stage embryonic hearts. Additionally, emerging spatial transcriptomics methods, such as the sequencing-based Visium HD[52] and Stereo-seq[53] and the imaging-based Xenium[54], offer more options. Visium HD and Stereo-seq have been reported to achieve subcellular spatial resolution, but the number of genes recovered per spot is relatively low. Bioinformatic approaches are therefore required to merge multiple spots for downstream analyses, which complicates the definition of cell boundaries and requires additional cell type deconvolution. Xenium can delineate cell boundaries using a cell segmentation kit, but both the transcript recovery per gene and the number of genes detected per cell remain relatively low. A new platform from Curio, called Trekker[55], can achieve true single-cell resolution by integrating in situ barcoding with single-nucleus mRNA sequencing; however, the experimental cost is high, and the method can only profile gene expression at the single-nucleus level. Overall, these new approaches offer better spatial resolution than the Visium method used in our study, but they come with significantly higher costs and may be challenging to apply to large tissue samples. In summary, each method has its own advantages and limitations, and the choice of platform depends on the specific experimental goals.

Through spatial pattern analysis of cell cycle phases, compact and trabecular gene modules, and the Myh6/Myh7 gene expression ratio, we found that mouse atrial CMs exhibit a more mature transcriptional signature compared to ventricular CMs. However, this does not necessarily indicate that atrial CMs are functionally more mature, as CM maturation is a complex process that must be assessed across multiple dimensions, including transcriptional, electrophysiological, metabolic, and contractile functions. Additionally, while mature human CMs are known to exhibit a lower *Myh6/Myh7* ratio[56], spatial transcriptomic analysis revealed a higher *Myh6/Myh7* ratio in atrial CMs compared to ventricular CMs, which contrasts with the

more mature transcriptional signature observed in mouse atrial CMs. This discrepancy warrants further investigation in future studies.

Through the analysis of Slide-seq data, we identified niche signals for conduction cells and EPDCs. We observed macroscopic signals, such as *Ptn* and *Mdk*, that influenced both the SAN and AVN. Additionally, we identified more localized signals, like *Fgf1* and *Tgfb1*, which primarily affected PF cells. Future functional experiments will be important to validate the roles of these signals in conduction system development. Moreover, it would be valuable to explore what regulates these niche signals. Given that signals may not originate from a single cell type, their development likely depends on specific environmental factors. Consistent with this idea, recent studies have shown that mechanical force can induce TNFα expression in the cardiac border zone after heart injury[57].

Unlike scRNA-seq analysis, spatial transcriptomic data preserves the original spatial context, allowing for the analysis of in situ niche signaling interactions. However, like scRNA-seq data, spatial transcriptomic data reflects gene expression at the transcriptional level. It remains unclear whether the transcriptional expression of genes in adjacent cells translates into protein interactions, and whether these interactions ultimately lead to functional outcomes. To address these questions, high-throughput assays that measure gene interactions at the protein level and connect these interactions to functional readouts will be required. Additionally, transcriptomic sections taken from different positions within the same organ may include distinct anatomical structures. Because spatial transcriptomic experiments are costly, only a limited number of sections from each organ can typically be profiled, complicating comparisons across experimental conditions. Therefore, profiling multiple sections or ideally the entire organ will be essential in the future for achieving accurate comparative analyses.

Methods:

Experimental methods

Mouse strains

The animal studies were approved by the University of Pittsburgh Institutional Animal Care and Use Committee (IACUC). We have complied with all relevant ethical regulations for animal use. CD1 mice were purchased from Charles River Laboratories and bred to generate embryos and neonatal pups for the spatial transcriptomics experiments. The transgenic mice, including Wt1-CreERT2 (Strain #010912)[58], Rosa26-mTmG (Strain #007676)[59], Pdgfra-CreER (Strain #032770)[60], and ROSA26-eGFP-DTA (Strain #032087)[61], were obtained from the Jackson Laboratory. Animals were not differentiated by sex, both male and female mice were potentially included in the analysis. Adult mice were euthanized by cervical dislocation. Neonatal mice were euthanized by decapitation.

Lineage tracing and DTA ablation

For the lineage tracing experiments, we bred Wt1-CreERT2 heterozygous male mice with Rosa26-mTmG female homozygous mice and treated the pregnant mice with 200 µg of tamoxifen per gram of body weight (200 µg/g) at E10.5 and E11.5. The embryos were harvested at E14.5. For the ablation experiments, Wt1-CreERT2 heterozygous male mice were bred with Rosa26-DTA homozygous female mice. The pregnant mice were treated with 200 µg/g of

tamoxifen at E10.5 and harvested at E12.5. Tamoxifen was administered via oral gavage in both experiments. The collected embryonic hearts were directly embedded in OCT for sectioning.

Visium experimental procedure

The embryonic and neonatal mouse hearts were obtained from pregnant CD1 mice. After thorough washing, the freshly harvested hearts were embedded directly in OCT, sectioned at a thickness of 10 μm, and mounted onto Visium Spatial Gene Expression slides from 10x Genomics. Subsequent procedures were performed using reagents from the Visium kit, as previously described[62]. Briefly, the sections were first imaged using the EVOS M7000 Imaging System (AMF7000). Following imaging, the tissues were permeabilized for 13 minutes, and their mRNA was reverse transcribed into cDNA on the slides. The cDNA was then amplified for 16-20 cycles (stage dependent), before being used to generate indexed libraries with 16 amplification cycles.

Slide-seq experimental procedure

For Slide-seq experiments, the embryonic hearts from CD1 embryos, the lineage tracing experiments, and the ablation experiments were directly embedded in OCT and sectioned with a thickness of 10 μm. The spatial transcriptomics libraries were prepared with Curio Seeker Kit (Curio Bioscience) following the manufacturer's guidelines. Briefly, 10 μm heart sections were mounted on the 3 × 3 mm tile with DNA-barcoded mRNA capture beads. After hybridization, reverse transcription, and tissue clearing, the beads were resuspended and collected. cDNA library was then generated by second strand synthesis and cDNA amplification. Finally, sequencing library was constructed with the Nextera XT DNA Library Preparation Kit (Illumina, FC-131-1024) using index adapters provided by Curio Bioscience.

Sequencing

The Visium libraries were sequenced on the Illumina NextSeq 2000 at the Health Sciences Sequencing Core at UPMC Children's Hospital of Pittsburgh, while the Slide-seq libraries were sequenced on the NovaSeq 6000 platform at the UPMC Genome Center and NovaSeq X at Novogene.

Immunofluorescence staining

CD1 mouse hearts were harvested in PBS containing phosphatase inhibitor (P2850-1ML). They were subsequently fixed with 4% paraformaldehyde at 4 ℃ overnight and cut into 10 μm sections. The sections were blocked with blocking buffer (10% goat serum, 1% BSA, 0.1% Tween 20) at room temperature for 1 hour and stained with antibodies, including Phospho-Stat3 (Tyr705) (CST, 9145T, 1:100), Phospho-p44/42 MAPK (Erk1/2) (Thr202/Tyr204) (CST, 9101S, 1:100), and Phospho-SMAD1/5 (Ser463/465) (CST, 9516T, 1:100) at 4 ℃ overnight. Additionally, cultured GFP-positive AVC cells were fixed and blocked under the same conditions and stained with Ki-67 (Invitrogen, 41-5698-82, 1:200) at 4 ℃ overnight. On the second day, samples were incubated with fluorophore-conjugated secondary antibodies for 1 hour and then stained with DAPI for 10 minutes at room temperature. Moreover, CD1 mouse hearts were harvested in PBS for PDGFRα staining. The sections were blocked with blocking buffer (5% donkey serum, 1% BSA, 0.1% Tween-20) and then stained with a PDGFRα antibody (R&D, AF1062-SP, 1:500).

RNAscope

RNAscope was performed using the Multiplex Fluorescent Reagent Kit v2 (Advanced Cell Diagnostics, 323270) according to the manufacturer's instructions and as previously described (Deng et al., 2025). Briefly, mouse hearts were washed with 1× PBS, embedded in OCT, and cut into 10 μm sections. Sections were then fixed, followed by dehydration, hydrogen peroxide treatment, and protease IV treatment. Afterward, the samples were hybridized with gene-specific Z probes. Subsequently, the hybridization signal was amplified and visualized with TSA Vivid Fluorophores. Finally, the samples were stained with DAPI and mounted with ProLong Gold Antifade Mountant. Gene-specific Z probes used in this study included Mm-Sema3d-C2 (488111-C2), Mm-Efnb2-C2 (477671-C2), Mm-Upk3b-C3 (568561-C3), Mm-Lamc1-C2 (517451-C2), Mm-Npr3-C3 (502991-C3), and the eGFP-O4 probe (538851). In the Sema3d and Npr3 co-stained sections, the AVC regions in both control and mutant hearts were manually defined, and the Sema3d signal intensity was normalized to the DAPI intensity within the same region.

Co-culture of AVC fibroblast and surrounding cells

Pdgfra-CreER mice were crossed with Rosa26-mTmG mice and treated with tamoxifen at E9.5 and E10.5. Embryos were harvested at E14.5, and the AVC and surrounding regions were dissected and washed with 1× PBS. Tissues were digested with 0.25% Trypsin/EDTA (Gibco, 25200056) at 37 °C for 10 minutes, followed by the addition of an equal volume of collagenase A and B (Sigma, 10103578001, 11088807001), and incubated at 37 °C for another 10 minutes. Samples were collected by centrifugation at 300 × g for 5 minutes and resuspended in fibroblast growth medium (ATCC, PCS-201-030, PCS-201-040). GFP-positive cells from the AVC region were isolated by FACS (BD, Aria II), seeded onto 0.1% gelatin-coated coverslips in a 24-well plate, and co-cultured with surrounding cells seeded onto a 0.4-μm pore cell culture insert (Millicell, PIHP01250). Cells were treated with 1 μM CP-673451 (Selleckchem, S1536) or an equivalent amount of DMSO in fibroblast growth medium for 3 days. After treatment, cells were collected for cell proliferation analysis. All images were acquired using a confocal microscope (Olympus Fluoview 3000 or Nikon A1). Image processing and analysis were performed using FIJI[63]. Ki67 positive fibroblasts were manually counted, with the analysis blinded to treatment groups.

Statistical analysis

Statistical analyses were performed using GraphPad Prism (version 9.5.1). Data are presented as mean ± SD. Unpaired two-tailed Student's t-test was used for comparisons between two groups. Sample sizes and the number of biological replicates for each experiment are indicated in the corresponding figure legends.

Data analysis

Data Availability

The newly generated spatial transcriptomic data have been uploaded to the Gene Expression Omnibus (GEO) under the accession number GSE282547. The datasets have also been uploaded to the UCSC Genome Browser and can be accessed via the following links (https://cells-test.gi.ucsc.edu/?ds=mouse-dev-cardiac-spatial). The E8.5 and E9.5 spatial

transcriptomic data were downloaded from GEO with the accession number GSE197353[22]. The scRNA-seq data used for the deconvolution of the E8.5 and E9.5 spatial data were obtained from GEO under the accession number GSE126128[23], and the scRNA-seq data for deconvolution of other stages was from GSE193346[24]. The conduction cell scRNA-seq data were downloaded from GSE132658[33]. The EPDC scRNA-seq data were obtained from GSE154715[47]. The Wt1 mutant and control scRNA-seq[24] data were sourced from GSE193346. The human spatial transcriptomic data were published before[19] and downloaded from https://data.mendeley.com/datasets/dgnysc3zn5/1.

Sequencing reads mapping and normalization

We acquired the unfiltered feature-barcode matrix for each sample by using Space Ranger (v2. 1. 0) 'count' command with manually selected dots and reorient-images enabled) on the demultiplexed FASTQ files and associated image, along with the prebuilt mm10 genome reference 2020-A. After it detected tissue, aligned reads, generated feature-spot matrices, and positioned spots, we then used Seurat[64] for all further analyses. In each slide, Seurat objects were created by Load10X_Spatial function and then normalized with natural-log transformation using log1p.

Similarly, we obtained the unfiltered matrix of curio Slide-seq data by using Curio seeker (v2.0) with custom GRCm38 genome reference (added eGFP sequence). Specifically, Curio seeker was first used to extract bead and molecular barcodes for the raw FASTQ files of each sample and filter beads obtained from sequencing data against the bead barcode whitelist. After filtering out beads with hamming distance greater than 2 and creating new Seurat objects, we manually normalized counts with natural log.

Section splitting

We split out the Visium images which have more than one tissue. We cut segments based on exact positions. After subsetting, we can visualize the certain stage cells either on the full image, or a cropped image. Stage E11.5, P0, E14.5, E16.5, E17_E11, and P2_E14 have multiple tissues in one image. In Curio seq samples, we first set filter range of each coordinate and then stored the shrank image in a new Seurat object.

Deconvolution analysis

Cell2Location (v0.1.3)[51] was used to decompose the Visium dataset spatial count matrix into a predefined set of reference cell signatures by modeling the matrix as a negative binomial distribution. In the analysis of Visium data, the model was trained by the following parameter settings: max_epochs = 30000, batch_size = None, and train_size = 1. GitHub: https://github.com/BayraktarLab/cell2location. After extracting the deconvolution result, CARD was used as a visualization tool to draw the pie charts[65].

RCTD[66] was used to leverage cell type profiles from scRNA-seq data to decompose mixtures which observed in spatial dataset. In the analysis of Curio Slide-seq data, the cell-type composition per dot was deconvolved using RCTD with the default settings. The reference consisted of cell types that were manually annotated from the Seurat object of the corresponding scRNA-seq data. GitHub :https://github.com/dmcable/spacexr, which is integrated into an R package called spacexr (v2.2.1).

COMMOT spatial ligand-receptor analysis of Visium data

We explored intercellular communication and the specificity of signal directionality within a spatial context, while also examining the impact on downstream genes. This was done by using COMMOT (v0.0.3)[29] to analyze cell-cell interactions. When analyzing Visium data, COMMOT identified the most active spatially colocalized ligand-receptor pairs, which were taken from the CellChat database.

Selection and ligand-receptor analysis of the Niche signal

To further analyze intercellular interactions at close distance, we utilized semla[67] to find the radial distance area around the target gene, calculates LRscores based on target gene expression information and surrounding area, and maps results onto spatial distribution. To identify the single layer of cells that surrounds the target cells, we set the r_dist_sqrt <20 or 30 (details in the provided code scripts).

Ligand-receptor interaction analysis in scRNA-seq data

CellChat (Version 2.1.0)[68] was used to analyze ligand-receptor interactions in the scRNA-seq data with the default settings. Specifically, CellChat was first used to examine interactions between different cardiac cell types using multi-stage scRNA-seq data[24], and the interactions of the PDGF and BMP pathways were plotted. Next, we analyzed the interactions between conduction cells and other cell types using micro-dissected tissue-derived scRNA-seq data[33].

NicheNet analysis

NicheNet[69] was used to analyze downstream target genes following the previously described procedure [24]. Briefly, we used scRNA-seq data from Wt1 mutant and control hearts at E14.5, considering Ven_CM cells as receiver cells and fibroblasts as sender cells. We then applied the NicheNet pipeline with default parameters to identify regulatory interactions and generate the plots.

The score of cell cycle phase, compact and trabecular, and LA and RA CM identities

The CellcycleScoring function in Seurat was used to score cell cycle phases in the spatial transcriptomic data based on the expression of a set of canonical marker genes provided by Seurat[64]. To annotate the identities of compact and trabecular CMs, we performed differential expression analysis on scRNA-seq data from compact and trabecular CMs, identifying the top 500 differentially expressed genes (Supplementary Dataset 1). We then used CellcycleScoring to score their identities. Additionally, we identified genes differentially expressed in LA and RA CMs (Supplementary Dataset 2) and used this information to annotate the spatial transcriptomic data with CellcycleScoring.

Human spatial transcriptomic data analysis

Human spatial transcriptomic data from pcw 6.5 and 9 were obtained from a previous study (Asp et al., 2019) and deconvolved using RCTD, based on human heart scRNA-seq data from pcw 6.5–7 from the same study. Cell type and gene expression plots were generated using Seurat. Cell cycle phase and compact/trabecular region assignments were performed using the CellCycleScoring function in Seurat. The genes used for the assignments were converted from the mouse genes listed above. Ligand–receptor interaction analysis was conducted with COMMOT in Python.

Acknowledgements

We'd like to thank all the members in the Li laboratory for their insightful discussions of this work and thank Dr. Zibei Gao for her help in staining Pdgfra on heart sections. We are also thankful to the Health Sciences Sequencing Core at UPMC Children's Hospital of Pittsburgh, Rangos Research Center (RRID:SCR_023116) for their assistance in processing the Visium samples. We are also grateful to the Center for Biologic Imaging (CBI) at the University of Pittsburgh for their support in imaging the stained samples. This research was supported in part by the University of Pittsburgh Center for Research Computing, RRID:SCR_022735, through the resources provided. Specifically, this work used the HTC cluster, which is supported by NIH award number S10OD028483.

Sources of Funding

This work was supported by R00HL133472 and DP2HL163745 from the NIH, Additional Ventures SVRF grant 1291906, and the CMRF grant from the University of Pittsburgh (G.L.). It was also supported in part by P01AI106684 and NSF2225775 (W.C.).

Author Contributions

J.H., H.H., and G.L. designed the experiments; J.X. bred the mice and harvested mouse hearts. J.H. and J.X. profiled the Slide-seq data. W.M. profiled the Visium data. H.H., J.H., and G.L. analyzed the spatial transcriptomic and scRNA-seq data; J.H. conducted the immunofluorescence and cell co-culture experiments; Y.H. performed the RNAscope experiments; T.L. and W.C. provided guidance on the spatial data analysis. J.H., H.H., and G.L. prepared the manuscript. All the authors edited the manuscript.

Code Availability

The computer code utilized to produce the results presented in this study is available on Zenodo, accessible via DOI: 10.5281/zenodo.14341430[70].

Competing interests

The authors declare no competing interests.

Figure legends:

Fig 1: Overview of the spatial transcriptomic atlas of mouse developing hearts. (A) Diagram of the experimental workflow that was used to profile the hearts at early stages with Slide-seq and the early and late stages with Visium. The diagram was created with BioRender. (B) The representative results of Slide-seq spatial data annotated with cell type information. (C) The representative pie chart plots showing the proportion of cell types in each Visium dot at different stages.

Fig 2: The spatial pattern of cells at different cell cycle phases and with expression of compact and trabecular identity genes. (A) Diagram of the data analysis procedure. (B) The spatial plots of Slide-seq data labeled by cell cycle phases at different stages. (C) The spatial plots of Slide-

seq data labeled by compact and trabecular identities at different stages. (D) The Visium data labeled by cell cycle phases. (E) The Visium data labeled by the identities of compact and trabecular myocardium. (F) The representative plots of Nppa expression at different stages of Visium data.

Fig 3: The spatial pattern of genes differentially expressing in chambers. (A) The spatial expression pattern of LA and RA-specific gene modules. (B, C) The expression pattern of representative LA and RA specific gene Adamts8 and Bmp10 at different stages of Visium data. (D) The dynamic expression pattern of *Myh6* and *Myh7* along the developmental progression. (E) The ratio of *Myh6* and *Myh7* in ACM and VCM at different stages.

Fig 4: The spatial pattern of ligand-receptor interactions through the analysis of Visium data. (A) The spatial distribution of global interaction intensities at different stages. (B) Circle plot showing the interaction of Pdgf pathway among different cell types. (C) Dot plot showing the detailed interactions. (D) Violin plot showing the expression of ligand and receptors at different cell types. (E) The pattern of Pdgf pathway activity. (F) The activity pattern of Pdgfa_Pdgfra interaction at different stages. (G) The expression pattern of Pdgf pathway downstream genes including positively and negatively regulated genes.

Fig 5: Interaction analysis of cardiac neuronal cells and their surrounding cells. (A) UMAP plot of embryonic SA node scRNA-seq data labeled with cell type information. (B, C) The expression pattern of SAN gene Hcn4 and neuronal gene Phox2b. (D, E) The top interactions between the other cell types derived ligands and SAN or neuron expressed receptors. (F) The spatial expression pattern of Shox2 and Phox2b. (G) The spatial pattern of representative ligands. (H) UMAP plot of Purkinje Fiber scRNA-seq data labeled with cell type information. (I) The expression pattern of representative PF gene Gja5 and Cacna2d2. (J) Identification of PF and their surrounding cells through the expression of a combination of marker genes. The PF cells were labeled green, the one layer of surrounding cells labeled yellow, and the rest outside cells were grey. (K) The top signaling interactions with surrounding cells derived ligands on PF target cells. (L) Spatial expression pattern of representative ligand Fgf1 and Tgfb1 that were shared in the two E14 expression slides.

Fig 6: In situ analysis of the interactions of EPDCs and their surrounding cells. (A) Diagram of the experimental workflow. The diagram was created with BioRender. (B) Lineage analysis of the EPDCs using *Wt1-CreER; Rosa26-mTmG* mice and confirmed the tracing results with tissue sectioning and imaging. (C) The main EPDC types in the scRNA-seq data of *Wt1-CreER; Rosa-mTmG* at E12.5 and E16.5. (D) The expression pattern of representative cell type-specific genes. (E) The spatial pattern of eGFP expression and the pattern of *eGFP*+ cells. (F) The spatial location of eGFP labeled EPDC subpopulations. (G) The top signals from surrounding cells to each EPDC populations.

Fig 7: Spatial transcriptomic analysis of the embryonic hearts with epicardium ablation. (A) Diagram of the experimental workflow and representative images of mouse embryos and embryonic hearts from control and *Wt1-CreER; Rosa-DTA* ablation mice. Scale bar = 1 mm. (B) Control and ablated hearts labeled with compact and trabecular myocardium identities. (C) Expression pattern of *Sox9* in control and ablated hearts. (D) The ligands in Fbs and their predicted target genes in Ven_CM that were differentially expressed at control and *Wt1* mutant at E14.5. (E) The expression pattern of ligand Inhba at control and ablated hearts. (F) The target gene Vim had reduced expression in ablated hearts than control hearts. (G) Expression pattern of the signaling molecule Sema3d in control and ablated hearts. (H) RNA staining of *Sema3d* and *Npr3* in control and ablated hearts. (I) Quantification of the ratio of *Sema3d* signal

to DAPI signal in the AVC regions of control and mutant hearts. Mean values with SD were plotted in the panel. N = 3 biological replicates. Statistical significance was determined by two-tailed *t*-test. p = 0.0015. Scale bar = 100 μm.

Legend for Supplementary Datasets:

Supplementary Dataset 1: The list of compact and trabecular myocardium genes for single cell annotation.

Supplementary Dataset 2: The top 20 differentially expressed genes in LA and RA CMs.

Supplementary Dataset 3: The p-value of ligand-receptor interactions between target cells and surrounding cells at different stages.

Supplementary Dataset 4: The mean of ligand-receptor interaction strengths between target cells and surrounding cells at different stages.

Supplementary Dataset 5: The p-value of ligand-receptor interactions between eGFP positive EPDCs and surrounding cells at e14.5_2 section.

Supplementary Dataset 6: The mean of ligand-receptor interaction strengths between eGFP positive EPDCs and surrounding cells at e14.5_2 section.

Supplementary Dataset 7: The p-value of ligand-receptor interactions between eGFP positive EPDCs and surrounding cells at e14.5_1 section.

Supplementary Dataset 8: The mean of ligand-receptor interaction strengths between eGFP positive EPDCs and surrounding cells at e14.5_1 section.

Supplementary Dataset 9: The group of ligands that have interactions with p-value less than 0.05 between compact CMs and surrounding cells in control and *Wt1-CreER;Rosa-DTA* mutants.

Supplementary Dataset 10: The group of ligands that have interactions with p-value less than 0.05 between trabecular CMs and surrounding cells in control and *Wt1-CreER;Rosa-DTA* mutants.

Supplementary Dataset 11: The group of ligands that have interactions with p-value less than 0.05 between endocardial endothelial cells and surrounding cells in control and *Wt1-CreER;Rosa-DTA* mutants.

Supplementary Dataset 12: Numerical source data for Supplementary Fig. 8D and Fig. 7I.

References:

1 Tallquist, M. D. Developmental Pathways of Cardiac Fibroblasts. *Cold Spring Harb Perspect Biol* **12**, doi:10.1101/cshperspect.a037184 (2020).

2 Trimm, E. & Red-Horse, K. Vascular endothelial cell development and diversity. *Nat Rev Cardiol* **20**, 197-210, doi:10.1038/s41569-022-00770-1 (2023).

3 Buckingham, M., Meilhac, S. & Zaffran, S. Building the mammalian heart from two sources of myocardial cells. *Nat Rev Genet* **6**, 826-835, doi:10.1038/nrg1710 (2005).

4 Evans, S. M., Yelon, D., Conlon, F. L. & Kirby, M. L. Myocardial lineage development. *Circ Res* **107**, 1428-1444, doi:10.1161/CIRCRESAHA.110.227405 (2010).

5 Rudolph, A. M. Myocardial growth before and after birth: clinical implications. *Acta Paediatr* **89**, 129-133, doi:10.1080/080352500750028681 (2000).

6 Gunthel, M., Barnett, P. & Christoffels, V. M. Development, Proliferation, and Growth of the Mammalian Heart. *Mol Ther* **26**, 1599-1609, doi:10.1016/j.ymthe.2018.05.022 (2018).

7 Fisher, S. A., Langille, B. L. & Srivastava, D. Apoptosis during cardiovascular development. *Circ Res* **87**, 856-864, doi:10.1161/01.res.87.10.856 (2000).

8 Christoffels, V. M. & Moorman, A. F. Development of the cardiac conduction system: why are some regions of the heart more arrhythmogenic than others? *Circ Arrhythm Electrophysiol* **2**, 195-207, doi:10.1161/CIRCEP.108.829341 (2009).

9 Rentschler, S. *et al.* Visualization and functional characterization of the developing murine cardiac conduction system. *Development* **128**, 1785-1792, doi:10.1242/dev.128.10.1785 (2001).

10 Choquet, C., Boulgakoff, L., Kelly, R. G. & Miquerol, L. New Insights into the Development and Morphogenesis of the Cardiac Purkinje Fiber Network: Linking Architecture and Function. *J Cardiovasc Dev Dis* **8**, doi:10.3390/jcdd8080095 (2021).

11 Giannino, G. *et al.* The Intrinsic Cardiac Nervous System: From Pathophysiology to Therapeutic Implications. *Biology (Basel)* **13**, doi:10.3390/biology13020105 (2024).

12 Cao, Y., Duca, S. & Cao, J. Epicardium in Heart Development. *Cold Spring Harb Perspect Biol* **12**, doi:10.1101/cshperspect.a037192 (2020).

13 Quijada, P., Trembley, M. A. & Small, E. M. The Role of the Epicardium During Heart Development and Repair. *Circ Res* **126**, 377-394, doi:10.1161/CIRCRESAHA.119.315857 (2020).

14 von Gise, A. *et al.* WT1 regulates epicardial epithelial to mesenchymal transition through beta-catenin and retinoic acid signaling pathways. *Dev Biol* **356**, 421-431, doi:10.1016/j.ydbio.2011.05.668 (2011).

15 Xu, J., Deng, Y. & Li, G. Keratin 19 (Krt19) is a novel marker gene for epicardial cells. *Front Genet* **15**, 1385867, doi:10.3389/fgene.2024.1385867 (2024).

16 von Gise, A. & Pu, W. T. Endocardial and epicardial epithelial to mesenchymal transitions in heart development and disease. *Circ Res* **110**, 1628-1645, doi:10.1161/CIRCRESAHA.111.259960 (2012).

17 Paik, D. T., Cho, S., Tian, L., Chang, H. Y. & Wu, J. C. Single-cell RNA sequencing in cardiovascular development, disease and medicine. *Nat Rev Cardiol* **17**, 457-473, doi:10.1038/s41569-020-0359-y (2020).

18 Williams, C. G., Lee, H. J., Asatsuma, T., Vento-Tormo, R. & Haque, A. An introduction to spatial transcriptomics for biomedical research. *Genome Med* **14**, 68, doi:10.1186/s13073-022-01075-1 (2022).

19 Asp, M. *et al.* A Spatiotemporal Organ-Wide Gene Expression and Cell Atlas of the Developing Human Heart. *Cell* **179**, 1647-1660 e1619, doi:10.1016/j.cell.2019.11.025 (2019).

20 Mantri, M., Zhang, H. H., Spanos, E., Ren, Y. A. & De Vlaminck, I. A spatiotemporal molecular atlas of the ovulating mouse ovary. *Proc Natl Acad Sci U S A* **121**, e2317418121, doi:10.1073/pnas.2317418121 (2024).

21 Farah, E. N. *et al.* Spatially organized cellular communities form the developing human heart. *Nature* **627**, 854-864, doi:10.1038/s41586-024-07171-z (2024).

22 Sampath Kumar, A. *et al.* Spatiotemporal transcriptomic maps of whole mouse embryos at the onset of organogenesis. *Nat Genet* **55**, 1176-1185, doi:10.1038/s41588-023-01435-6 (2023).

23 de Soysa, T. Y. *et al.* Single-cell analysis of cardiogenesis reveals basis for organ-level developmental defects. *Nature* **572**, 120-124, doi:10.1038/s41586-019-1414-x (2019).

24 Feng, W. *et al.* Single-cell transcriptomic analysis identifies murine heart molecular features at embryonic and neonatal stages. *Nat Commun* **13**, 7960, doi:10.1038/s41467-022-35691-7 (2022).

25 Nestorowa, S. *et al.* A single-cell resolution map of mouse hematopoietic stem and progenitor cell differentiation. *Blood* **128**, e20-31, doi:10.1182/blood-2016-05-716480 (2016).

26 Li, G. *et al.* Single cell expression analysis reveals anatomical and cell cycle-dependent transcriptional shifts during heart development. *Development* **146**, doi:10.1242/dev.173476 (2019).

27 Buikema, J. W. *et al.* Wnt/beta-catenin signaling directs the regional expansion of first and second heart field-derived ventricular cardiomyocytes. *Development* **140**, 4165-4176, doi:10.1242/dev.099325 (2013).

28 Tian, X. *et al.* Identification of a hybrid myocardial zone in the mammalian heart after birth. *Nat Commun* **8**, 87, doi:10.1038/s41467-017-00118-1 (2017).

29 Cang, Z. *et al.* Screening cell-cell communication in spatial transcriptomics via collective optimal transport. *Nat Methods* **20**, 218-228, doi:10.1038/s41592-022-01728-4 (2023).

30 Makki, N., Thiel, K. W. & Miller, F. J., Jr. The epidermal growth factor receptor and its ligands in cardiovascular disease. *Int J Mol Sci* **14**, 20597-20613, doi:10.3390/ijms141020597 (2013).

31 McCulley, D. J., Kang, J. O., Martin, J. F. & Black, B. L. BMP4 is required in the anterior heart field and its derivatives for endocardial cushion remodeling, outflow tract septation, and semilunar valve development. *Dev Dyn* **237**, 3200-3209, doi:10.1002/dvdy.21743 (2008).

32 Rivera-Feliciano, J. & Tabin, C. J. Bmp2 instructs cardiac progenitors to form the heart-valve-inducing field. *Dev Biol* **295**, 580-588, doi:10.1016/j.ydbio.2006.03.043 (2006).

33 Goodyer, W. R. *et al.* Transcriptomic Profiling of the Developing Cardiac Conduction System at Single-Cell Resolution. *Circ Res* **125**, 379-397, doi:10.1161/CIRCRESAHA.118.314578 (2019).

34 Bartos, D. C., Grandi, E. & Ripplinger, C. M. Ion Channels in the Heart. *Compr Physiol* **5**, 1423-1464, doi:10.1002/cphy.c140069 (2015).

35 Choudhury, M., Boyett, M. R. & Morris, G. M. Biology of the Sinus Node and its Disease. *Arrhythm Electrophysiol Rev* **4**, 28-34, doi:10.15420/aer.2015.4.1.28 (2015).

36 van Eif, V. W. W., Stefanovic, S., Mohan, R. A. & Christoffels, V. M. Gradual differentiation and confinement of the cardiac conduction system as indicated by marker gene expression. *Biochim Biophys Acta Mol Cell Res* **1867**, 118509, doi:10.1016/j.bbamcr.2019.07.004 (2020).

37 van Eif, V. W. W. *et al.* Transcriptome analysis of mouse and human sinoatrial node cells reveals a conserved genetic program. *Development* **146**, doi:10.1242/dev.173161 (2019).

38 Dubreuil, V., Hirsch, M. R., Jouve, C., Brunet, J. F. & Goridis, C. The role of Phox2b in synchronizing pan-neuronal and type-specific aspects of neurogenesis. *Development* **129**, 5241-5253, doi:10.1242/dev.129.22.5241 (2002).

39 Engleka, K. A. *et al.* Islet1 derivatives in the heart are of both neural crest and second heart field origin. *Circ Res* **110**, 922-926, doi:10.1161/CIRCRESAHA.112.266510 (2012).

40 Chen, H. I. *et al.* The sinus venosus contributes to coronary vasculature through VEGFC-stimulated angiogenesis. *Development* **141**, 4500-4512, doi:10.1242/dev.113639 (2014).

41 Rasanen, M. *et al.* VEGF-B Promotes Endocardium-Derived Coronary Vessel Development and Cardiac Regeneration. *Circulation* **143**, 65-77, doi:10.1161/CIRCULATIONAHA.120.050635 (2021).

42 Fernandez-Martos, C. M., King, A. E., Atkinson, R. A., Woodhouse, A. & Vickers, J. C. Neurofilament light gene deletion exacerbates amyloid, dystrophic neurite, and synaptic pathology in the APP/PS1 transgenic model of Alzheimer's disease. *Neurobiol Aging* **36**, 2757-2767, doi:10.1016/j.neurobiolaging.2015.07.003 (2015).

43 Borghini, S. *et al.* The TLX2 homeobox gene is a transcriptional target of PHOX2B in neural-crest-derived cells. *Biochem J* **395**, 355-361, doi:10.1042/BJ20051386 (2006).

44 Menge, S., Decker, L. & Freischmidt, A. Restoring expression of Stathmin-2: a novel strategy to treat TDP-43 proteinopathies. *Signal Transduct Target Ther* **8**, 266, doi:10.1038/s41392-023-01533-1 (2023).

45 Goodyer, W. R. *et al.* In vivo visualization and molecular targeting of the cardiac conduction system. *J Clin Invest* **132**, doi:10.1172/JCI156955 (2022).

46 Dun, W. & Boyden, P. A. The Purkinje cell; 2008 style. *J Mol Cell Cardiol* **45**, 617-624, doi:10.1016/j.yjmcc.2008.08.001 (2008).

47 Quijada, P. *et al.* Coordination of endothelial cell positioning and fate specification by the epicardium. *Nat Commun* **12**, 4155, doi:10.1038/s41467-021-24414-z (2021).

48 Su, S. A. *et al.* Essential roles of EphrinB2 in mammalian heart: from development to diseases. *Cell Commun Signal* **17**, 29, doi:10.1186/s12964-019-0337-3 (2019).

49 Malan, D. *et al.* Lack of laminin gamma1 in embryonic stem cell-derived cardiomyocytes causes inhomogeneous electrical spreading despite intact differentiation and function. *Stem Cells* **27**, 88-99, doi:10.1634/stemcells.2008-0335 (2009).

50 Pollitt, E. J. G., Sanchez-Posada, J., Snashall, C. M., Derrick, C. J. & Noel, E. S. Llgl1 mediates timely epicardial emergence and establishment of an apical laminin sheath around the trabeculating cardiac ventricle. *Development* **151**, doi:10.1242/dev.202482 (2024).

51 Kleshchevnikov, V. *et al.* Cell2location maps fine-grained cell types in spatial transcriptomics. *Nat Biotechnol* **40**, 661-671, doi:10.1038/s41587-021-01139-4 (2022).

52 Oliveira, M. F. *et al.* High-definition spatial transcriptomic profiling of immune cell populations in colorectal cancer. *Nat Genet* **57**, 1512-1523, doi:10.1038/s41588-025-02193-3 (2025).

53 Chen, A. *et al.* Spatiotemporal transcriptomic atlas of mouse organogenesis using DNA nanoball-patterned arrays. *Cell* **185**, 1777-1792 e1721, doi:10.1016/j.cell.2022.04.003 (2022).

54 Janesick, A. *et al.* High resolution mapping of the tumor microenvironment using integrated single-cell, spatial and in situ analysis. *Nat Commun* **14**, 8353, doi:10.1038/s41467-023-43458-x (2023).

55 Russell, A. J. C. *et al.* Slide-tags enables single-nucleus barcoding for multimodal spatial genomics. *Nature* **625**, 101-109, doi:10.1038/s41586-023-06837-4 (2024).

56 Guo, Y. & Pu, W. T. Cardiomyocyte Maturation: New Phase in Development. *Circ Res* **126**, 1086-1106, doi:10.1161/CIRCRESAHA.119.315862 (2020).

57 Ninh, V. K. *et al.* Spatially clustered type I interferon responses at injury borderzones. *Nature* **633**, 174-181, doi:10.1038/s41586-024-07806-1 (2024).

58 Zhou, B. *et al.* Epicardial progenitors contribute to the cardiomyocyte lineage in the developing heart. *Nature* **454**, 109-113, doi:10.1038/nature07060 (2008).

59 Muzumdar, M. D., Tasic, B., Miyamichi, K., Li, L. & Luo, L. A global double-fluorescent Cre reporter mouse. *Genesis* **45**, 593-605, doi:10.1002/dvg.20335 (2007).

60 Chung, M. I., Bujnis, M., Barkauskas, C. E., Kobayashi, Y. & Hogan, B. L. M. Niche-mediated BMP/SMAD signaling regulates lung alveolar stem cell proliferation and differentiation. *Development* **145**, doi:10.1242/dev.163014 (2018).

61 Ivanova, A. *et al.* In vivo genetic ablation by Cre-mediated expression of diphtheria toxin fragment A. *Genesis* **43**, 129-135, doi:10.1002/gene.20162 (2005).

62 He, K. *et al.* Spatial microniches of IL-2 combine with IL-10 to drive lung migratory T(H)2 cells in response to inhaled allergen. *Nat Immunol* **25**, 2124-2139, doi:10.1038/s41590-024-01986-8 (2024).

63 Schindelin, J. *et al.* Fiji: an open-source platform for biological-image analysis. *Nat Methods* **9**, 676-682, doi:10.1038/nmeth.2019 (2012).

64 Hao, Y. *et al.* Dictionary learning for integrative, multimodal and scalable single-cell analysis. *Nat Biotechnol* **42**, 293-304, doi:10.1038/s41587-023-01767-y (2024).

65 Ma, Y. & Zhou, X. Spatially informed cell-type deconvolution for spatial transcriptomics. *Nat Biotechnol* **40**, 1349-1359, doi:10.1038/s41587-022-01273-7 (2022).
66 Cable, D. M. *et al.* Robust decomposition of cell type mixtures in spatial transcriptomics. *Nat Biotechnol* **40**, 517-526, doi:10.1038/s41587-021-00830-w (2022).
67 Larsson, L., Franzen, L., Stahl, P. L. & Lundeberg, J. Semla: a versatile toolkit for spatially resolved transcriptomics analysis and visualization. *Bioinformatics* **39**, doi:10.1093/bioinformatics/btad626 (2023).
68 Jin, S. *et al.* Inference and analysis of cell-cell communication using CellChat. *Nat Commun* **12**, 1088, doi:10.1038/s41467-021-21246-9 (2021).
69 Browaeys, R., Saelens, W. & Saeys, Y. NicheNet: modeling intercellular communication by linking ligands to target genes. *Nat Methods* **17**, 159-162, doi:10.1038/s41592-019-0667-5 (2020).
70 Hu, J., He, H., Xu, J., MacDonald, W.A., He, Y., Liu, T., Chen, W., & Li, G. (2025). Spatial transcriptomic profiling of developing mouse hearts reveals a spatially patterned signaling environment. Zenodo. https://doi.org/10.5281/zenodo.14341430

Editor's Summary

The authors present spatial transcriptomics atlases of developing mouse hearts at embryonic and neonatal stages, complemented with ligand–receptor interaction analyses.

Peer review statement

Communications Biology thanks the anonymous reviewers for their contribution to the peer review of this work. Primary Handling Editor: Dario Ummarino.

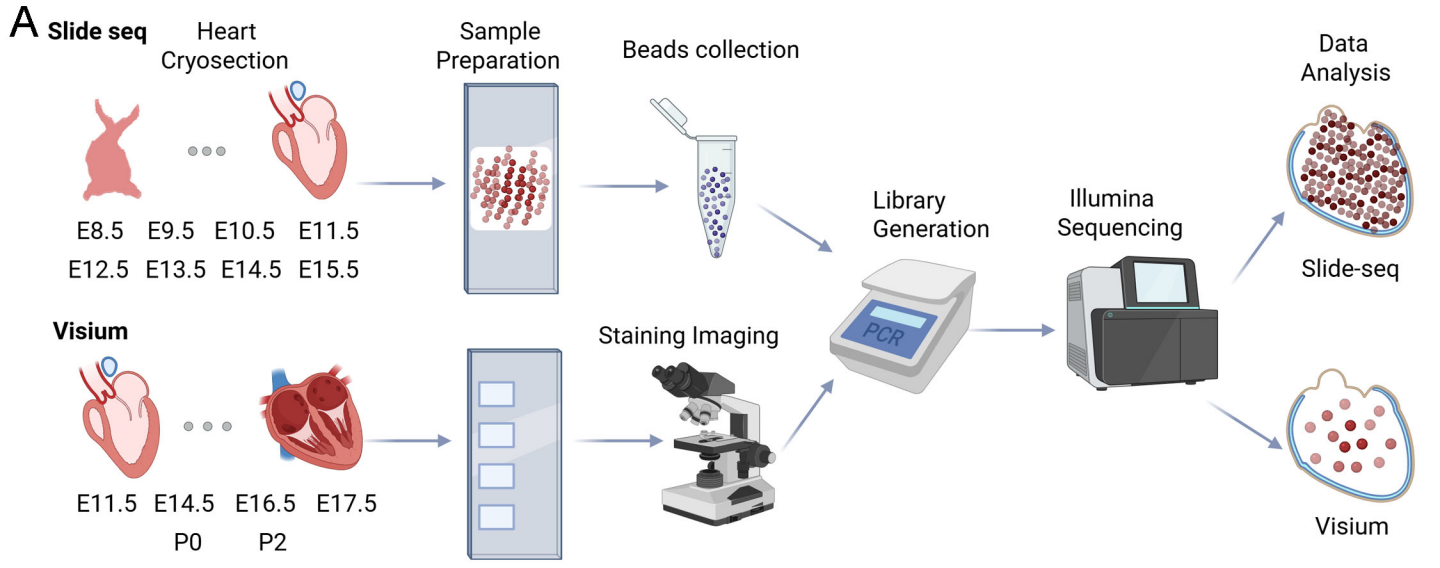
A
Slide seq
Heart Cryosection
Sample Preparation
Beads collection
Data Analysis
E8.5 E9.5 E10.5 E11.5
E12.5 E13.5 E14.5 E15.5
Library Generation
Illumina Sequencing
Slide-seq
Visium
Staining Imaging
PCR
E11.5 E14.5 E16.5 E17.5
P0 P2
Visium

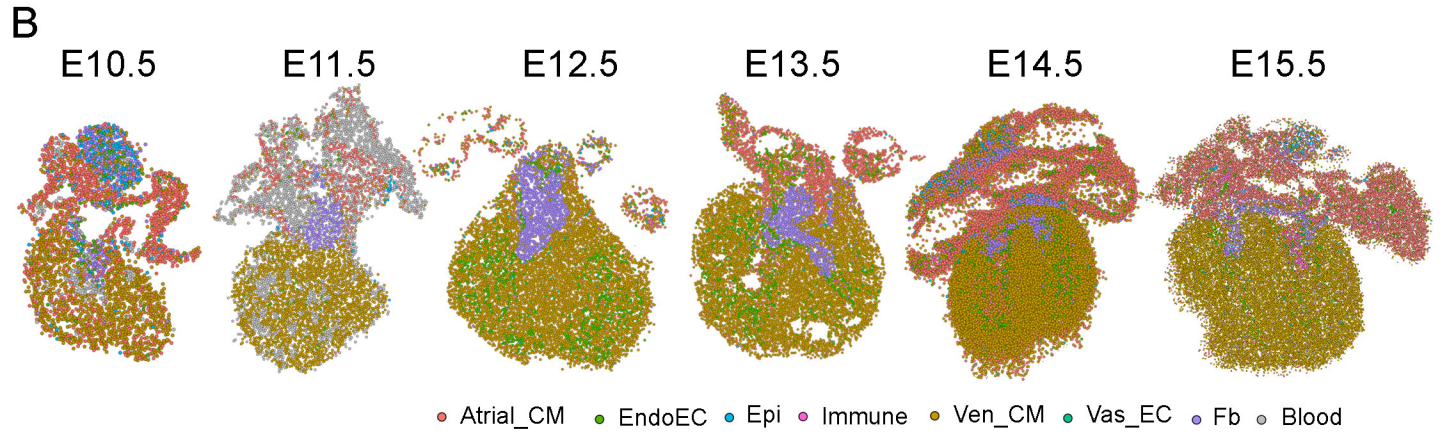
B
E10.5
E11.5
E12.5
E13.5
E14.5
E15.5
Atrial_CM
EndoEC
Epi
Immune
Ven_CM
Vas_EC
Fb
Blood

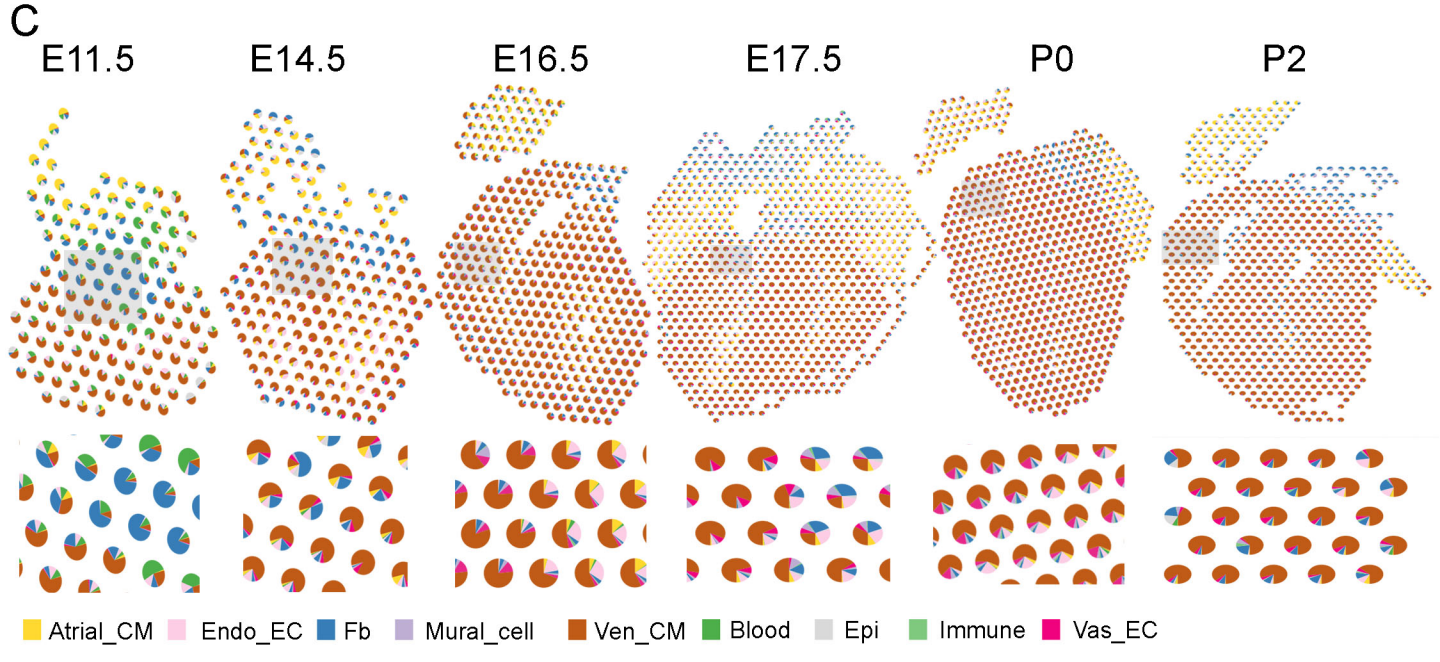
C
E11.5
E14.5
E16.5
E17.5
P0
P2
Atrial_CM
Endo_EC
Fb
Mural_cell
Ven_CM
Blood
Epi
Immune
Vas_EC

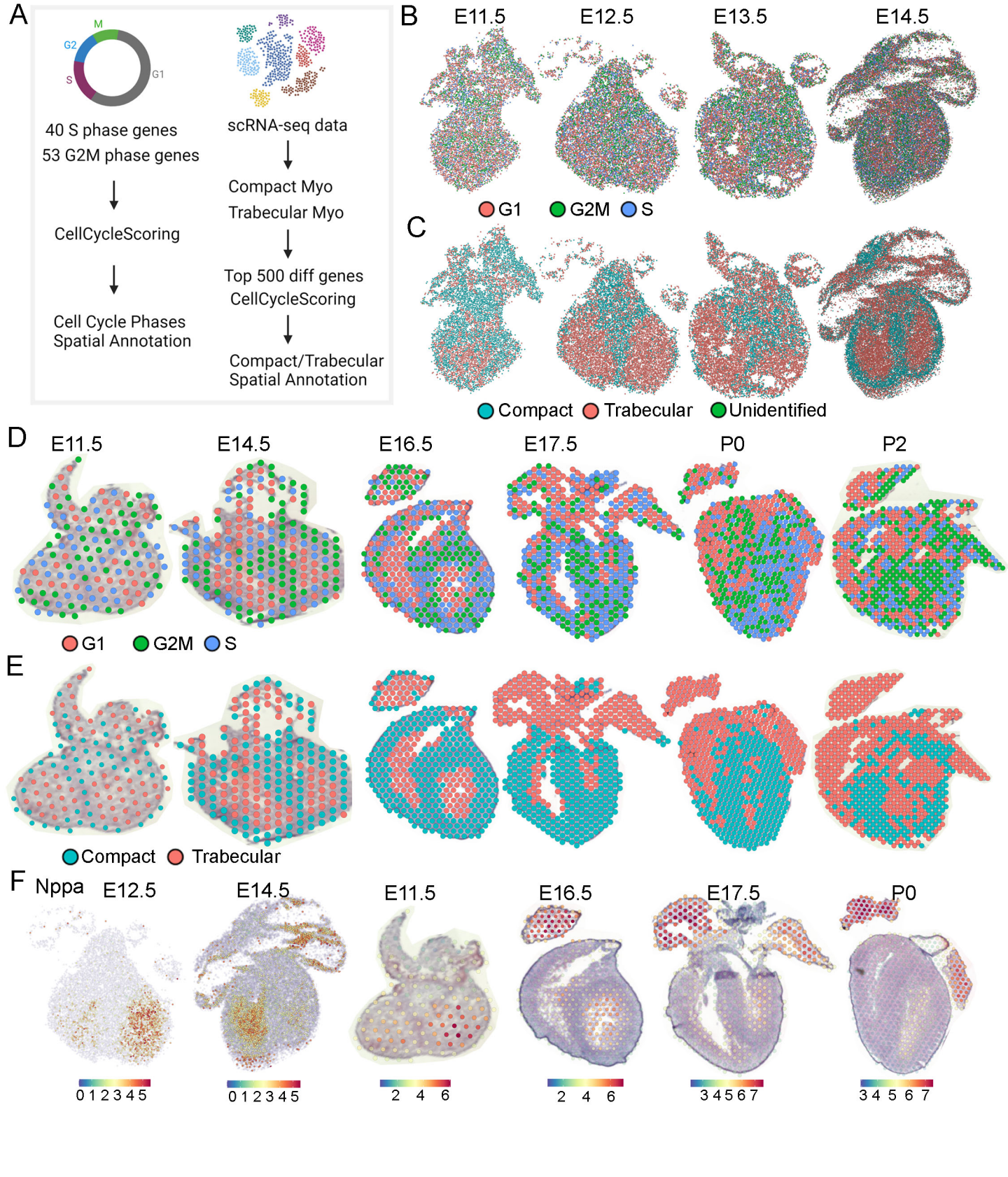
A
M
G2
S
G1
40 S phase genes
53 G2M phase genes
CellCycleScoring
Cell Cycle Phases
Spatial Annotation
scRNA-seq data
Compact Myo
Trabecular Myo
Top 500 diff genes
CellCycleScoring
Compact/Trabecular
Spatial Annotation
B
E11.5
E12.5
E13.5
E14.5
G1
G2M
S
C
Compact
Trabecular
Unidentified
D
E11.5
E14.5
E16.5
E17.5
P0
P2
G1
G2M
S
E
Compact
Trabecular
F
Nppa
E12.5
E14.5
E11.5
E16.5
E17.5
P0
0 1 2 3 4 5
0 1 2 3 4 5
2 4 6
2 4 6
3 4 5 6 7
3 4 5 6 7

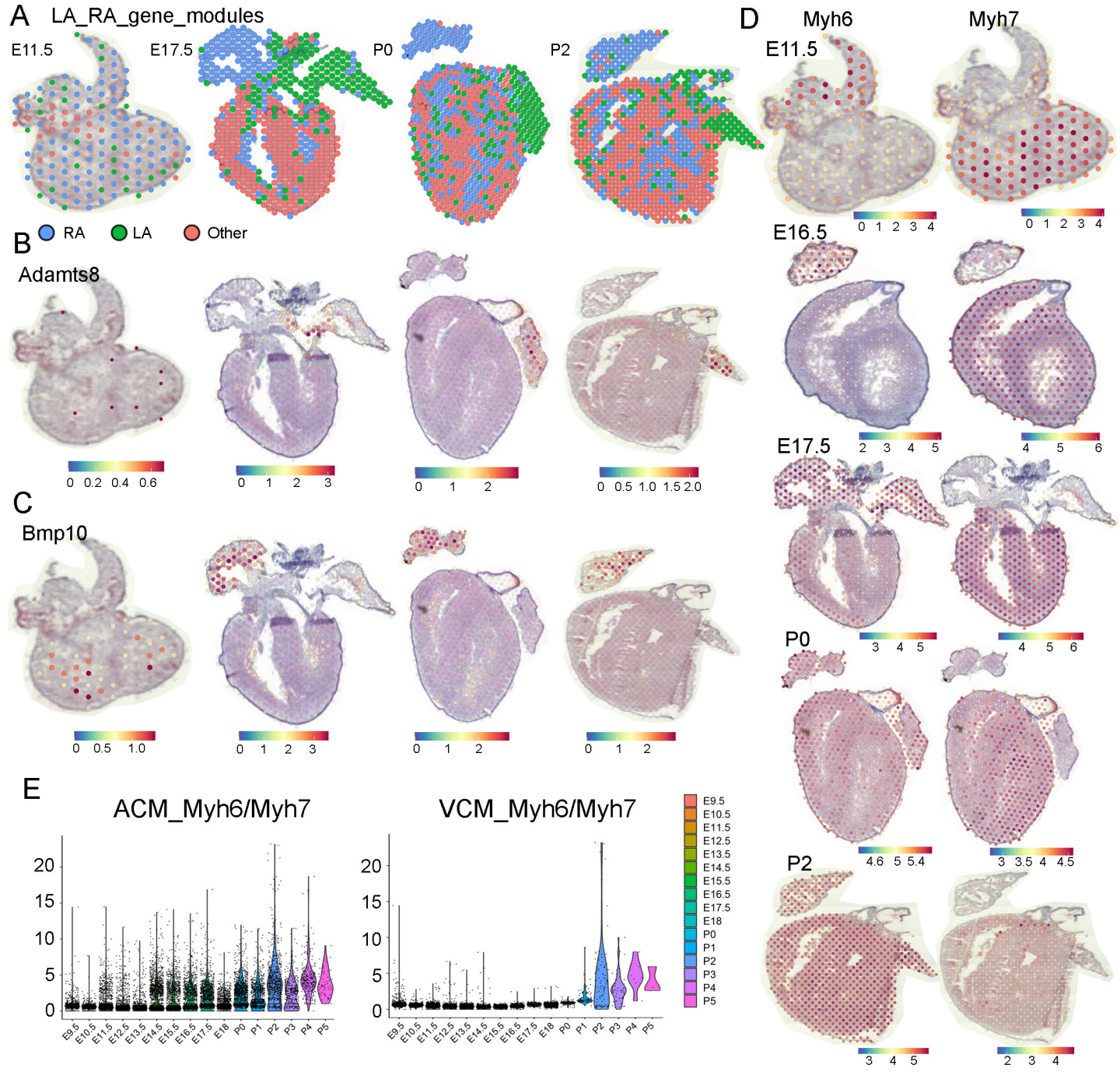
A
LA_RA_gene_modules
E11.5
E17.5
P0
P2
RA
LA
Other
B
Adamts8
0 0.2 0.4 0.6
0 1 2 3
0 1 2
0 0.5 1.0 1.5 2.0
C
Bmp10
0 0.5 1.0
0 1 2 3
0 1 2
0 1 2
D
Myh6
Myh7
E11.5
0 1 2 3 4
0 1 2 3 4
E16.5
2 3 4 5
4 5 6
E17.5
3 4 5
4 5 6
P0
4.6 5 5.4
3 3.5 4 4.5
P2
3 4 5
2 3 4
E
ACM_Myh6/Myh7
VCM_Myh6/Myh7
20
15
10
5
0
E9.5
E10.5
E11.5
E12.5
E13.5
E14.5
E15.5
E16.5
E17.5
E18
P0
P1
P2
P3
P4
P5

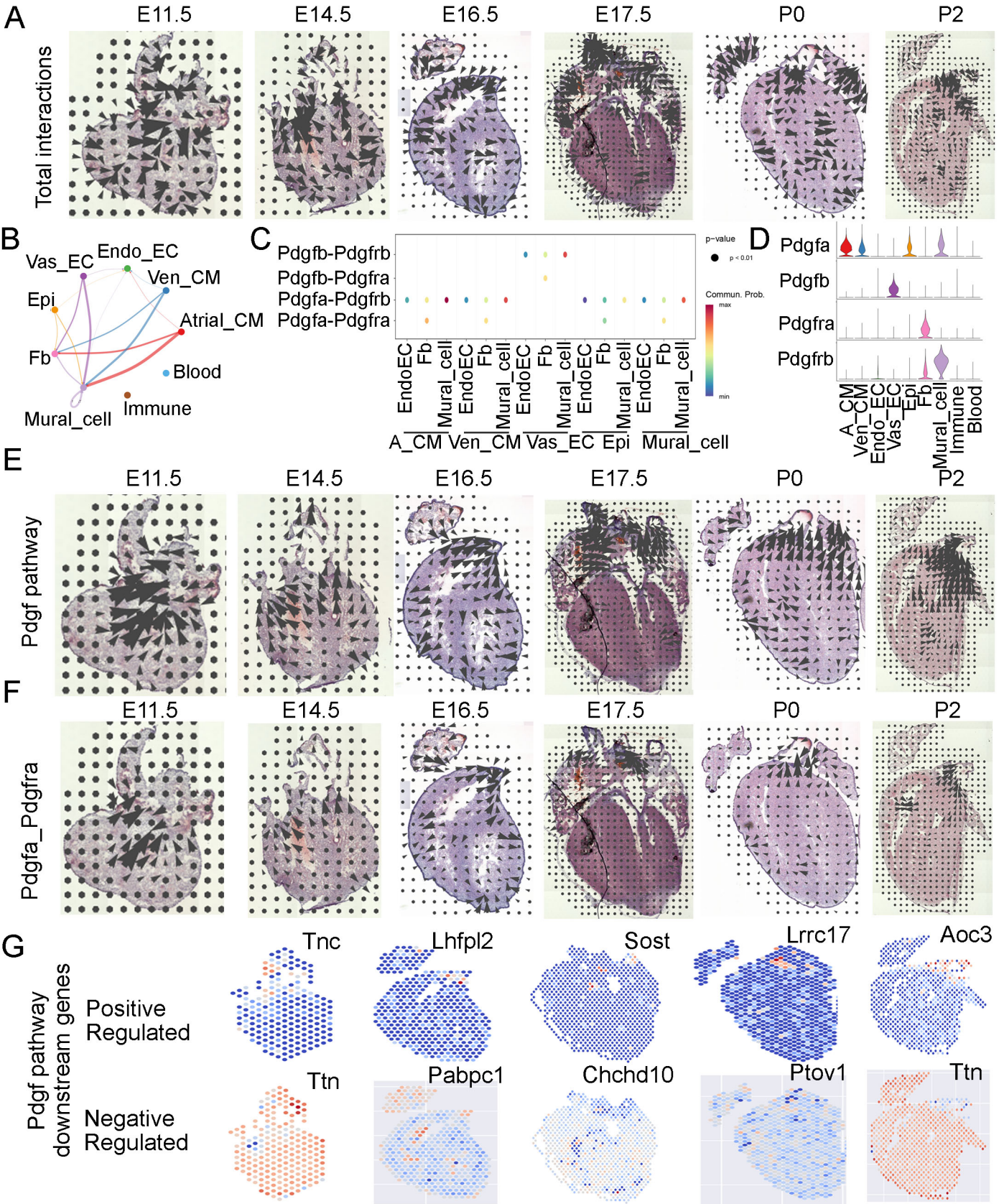
A
E11.5
E14.5
E16.5
E17.5
P0
P2
Total interactions
B
Vas_EC
Endo_EC
Ven_CM
Epi
Atrial_CM
Fb
Blood
Immune
Mural_cell
C
Pdgfb-Pdgfrb
Pdgfb-Pdgfra
Pdgfa-Pdgfrb
Pdgfa-Pdgfra
p-value
p < 0.01
Commun. Prob.
max
min
EndoEC
Fb
Mural_cell
A_CM
Ven_CM
Vas_EC
Epi
Mural_cell
D
Pdgfa
Pdgfb
Pdgfra
Pdgfrb
A_CM
Ven_CM
Endo_EC
Vas_EC
Epi
Fb
Mural_cell
Immune
Blood
E
E11.5
E14.5
E16.5
E17.5
P0
P2
Pdgf pathway
F
E11.5
E14.5
E16.5
E17.5
P0
P2
Pdgfa_Pdgfra
G
Pdgf pathway downstream genes
Positive Regulated
Negative Regulated
Tnc
Lhfpl2
Sost
Lrrc17
Aoc3
Ttn
Pabpc1
Chchd10
Ptov1
Ttn

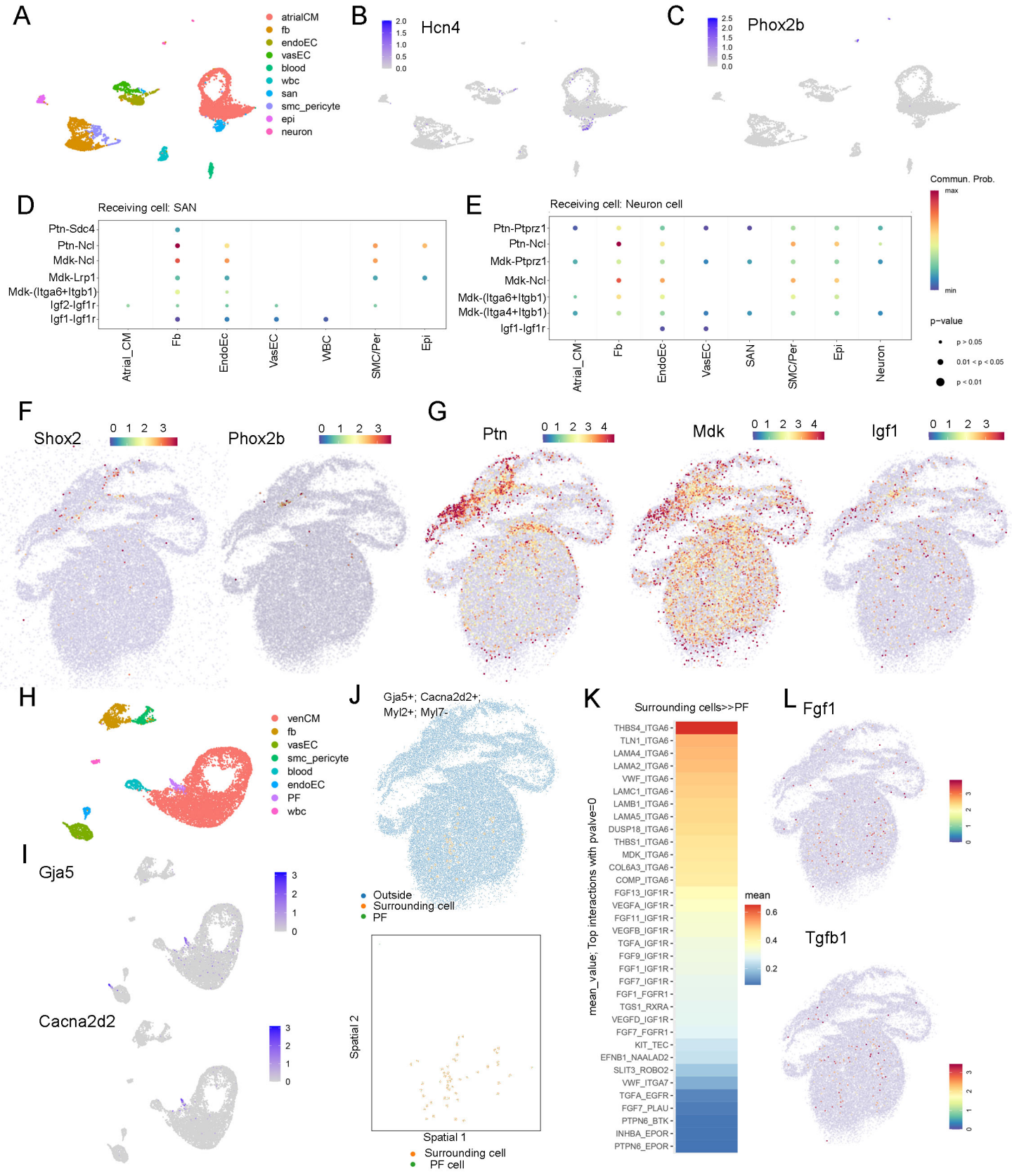
A
atrialCM
fb
endoEC
vasEC
blood
wbc
san
smc_pericyte
epi
neuron
B
Hcn4
C
Phox2b
D
Receiving cell: SAN
Ptn-Sdc4
Ptn-Ncl
Mdk-Ncl
Mdk-Lrp1
Mdk-(Itga6+Itgb1)
Igf2-Igf1r
Igf1-Igf1r
Atrial_CM
Fb
EndoEc
VasEC
WBC
SMC/Per
Epi
E
Receiving cell: Neuron cell
Ptn-Ptprz1
Ptn-Ncl
Mdk-Ptprz1
Mdk-Ncl
Mdk-(Itga6+Itgb1)
Mdk-(Itga4+Itgb1)
Igf1-Igf1r
Atrial_CM
Fb
EndoEc
VasEC
SAN
SMC/Per
Epi
Neuron
Commun. Prob.
max
min
p-value
p > 0.05
0.01 < p < 0.05
p < 0.01
F
Shox2
Phox2b
G
Ptn
Mdk
Igf1
H
venCM
fb
vasEC
smc_pericyte
blood
endoEC
PF
wbc
I
Gja5
Cacna2d2
J
Gja5+; Cacna2d2+;
Myl2+; Myl7-
Outside
Surrounding cell
PF
Spatial 1
Spatial 2
Surrounding cell
PF cell
K
Surrounding cells>>PF
mean_value; Top interactions with pvalue=0
THBS4_ITGA6
TLN1_ITGA6
LAMA4_ITGA6
LAMA2_ITGA6
VWF_ITGA6
LAMC1_ITGA6
LAMB1_ITGA6
LAMA5_ITGA6
DUSP18_ITGA6
THBS1_ITGA6
MDK_ITGA6
COL6A3_ITGA6
COMP_ITGA6
FGF13_IGF1R
VEGFA_IGF1R
FGF11_IGF1R
VEGFB_IGF1R
TGFA_IGF1R
FGF9_IGF1R
FGF1_IGF1R
FGF7_IGF1R
FGF1_FGFR1
TGS1_RXRA
VEGFD_IGF1R
FGF7_FGFR1
KIT_TEC
EFNB1_NAALAD2
SLIT3_ROBO2
VWF_ITGA7
TGFA_EGFR
FGF7_PLAU
PTPN6_BTK
INHBA_EPOR
PTPN6_EPOR
mean
L
Fgf1
Tgfb1

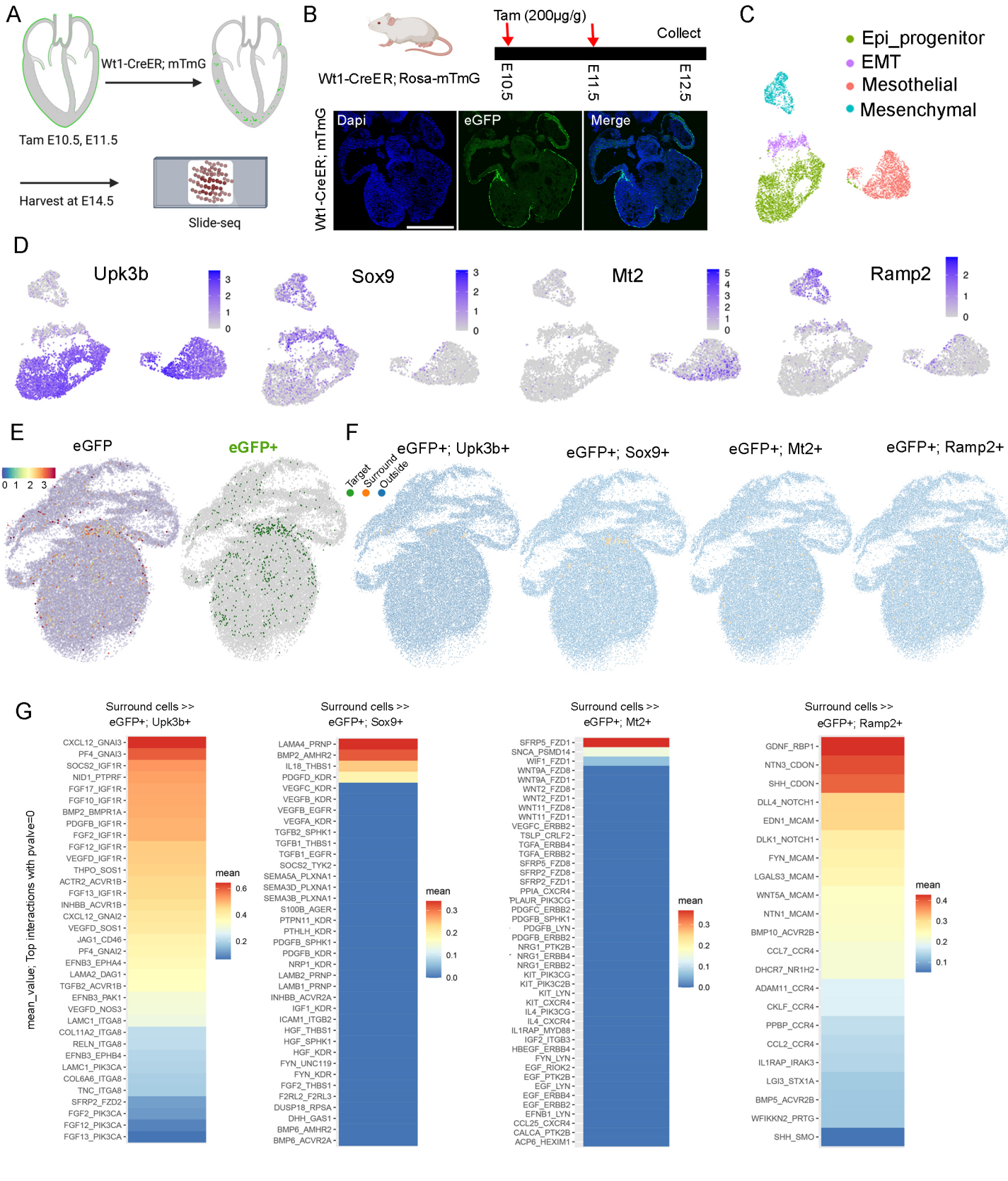
A
Wt1-CreER; mTmG
Tam E10.5, E11.5
Harvest at E14.5
Slide-seq
B
Wt1-CreER; Rosa-mTmG
Tam (200μg/g)
Collect
E10.5
E11.5
E12.5
Wt1-CreER; mTmG
Dapi
eGFP
Merge
C
Epi_progenitor
EMT
Mesothelial
Mesenchymal
D
Upk3b
Sox9
Mt2
Ramp2
E
eGFP
eGFP+
0 1 2 3
F
eGFP+; Upk3b+
eGFP+; Sox9+
eGFP+; Mt2+
eGFP+; Ramp2+
Target
Surround
Outside
G
Surround cells >>
eGFP+; Upk3b+
CXCL12_GNAI3
PF4_GNAI3
SOCS2_IGF1R
NID1_PTPRF
FGF17_IGF1R
FGF10_IGF1R
BMP2_BMPR1A
PDGFB_IGF1R
FGF2_IGF1R
FGF12_IGF1R
VEGFD_IGF1R
THPO_SOS1
ACTR2_ACVR1B
FGF13_IGF1R
INHBB_ACVR1B
CXCL12_GNAI2
VEGFD_SOS1
JAG1_CD46
PF4_GNAI2
EFNB3_EPHA4
LAMA2_DAG1
TGFB2_ACVR1B
EFNB3_PAK1
VEGFD_NOS3
LAMC1_ITGA8
COL11A2_ITGA8
RELN_ITGA8
EFNB3_EPHB4
LAMC1_PIK3CA
COL6A6_ITGA8
TNC_ITGA8
SFRP2_FZD2
FGF2_PIK3CA
FGF12_PIK3CA
FGF13_PIK3CA
mean
0.6
0.4
0.2
Surround cells >>
eGFP+; Sox9+
LAMA4_PRNP
BMP2_AMHR2
IL18_THBS1
PDGFD_KDR
VEGFC_KDR
VEGFB_KDR
VEGFB_EGFR
VEGFA_KDR
TGFB2_SPHK1
TGFB1_THBS1
TGFB1_EGFR
SOCS2_TYK2
SEMA5A_PLXNA1
SEMA3D_PLXNA1
SEMA3B_PLXNA1
S100B_AGER
PTPN11_KDR
PTHLH_KDR
PDGFB_SPHK1
PDGFB_KDR
NRP1_KDR
LAMB2_PRNP
LAMB1_PRNP
INHBB_ACVR2A
IGF1_KDR
ICAM1_ITGB2
HGF_THBS1
HGF_SPHK1
HGF_KDR
FYN_UNC119
FYN_KDR
FGF2_THBS1
F2RL2_F2RL3
DUSP18_RPSA
DHH_GAS1
BMP6_AMHR2
BMP6_ACVR2A
mean
0.3
0.2
0.1
0.0
Surround cells >>
eGFP+; Mt2+
SFRP5_FZD1
SNCA_PSMD14
WIF1_FZD1
WNT9A_FZD8
WNT9A_FZD1
WNT2_FZD8
WNT2_FZD1
WNT11_FZD8
WNT11_FZD1
VEGFC_ERBB2
TSLP_CRLF2
TGFA_ERBB4
TGFA_ERBB2
SFRP5_FZD8
SFRP2_FZD8
SFRP2_FZD1
PPIA_CXCR4
PLAUR_PIK3CG
PDGFC_ERBB2
PDGFB_SPHK1
PDGFB_LYN
PDGFB_ERBB2
NRG1_PTK2B
NRG1_ERBB4
NRG1_ERBB2
KIT_PIK3CG
KIT_PIK3C2B
KIT_LYN
KIT_CXCR4
IL4_PIK3CG
IL4_CXCR4
IL1RAP_MYD88
IGF2_ITGB3
HBEGF_ERBB4
FYN_LYN
EGF_RIOK2
EGF_PTK2B
EGF_LYN
EGF_ERBB4
EGF_ERBB2
EFNB1_LYN
CCL25_CXCR4
CALCA_PTK2B
ACP6_HEXIM1
mean
0.3
0.2
0.1
0.0
Surround cells >>
eGFP+; Ramp2+
GDNF_RBP1
NTN3_CDON
SHH_CDON
DLL4_NOTCH1
EDN1_MCAM
DLK1_NOTCH1
FYN_MCAM
LGALS3_MCAM
WNT5A_MCAM
NTN1_MCAM
BMP10_ACVR2B
CCL7_CCR4
DHCR7_NR1H2
ADAM11_CCR4
CKLF_CCR4
PPBP_CCR4
CCL2_CCR4
IL1RAP_IRAK3
LGI3_STX1A
BMP5_ACVR2B
WFIKKN2_PRTG
SHH_SMO
mean
0.4
0.3
0.2
0.1
mean_value; Top interactions with pvalve=0

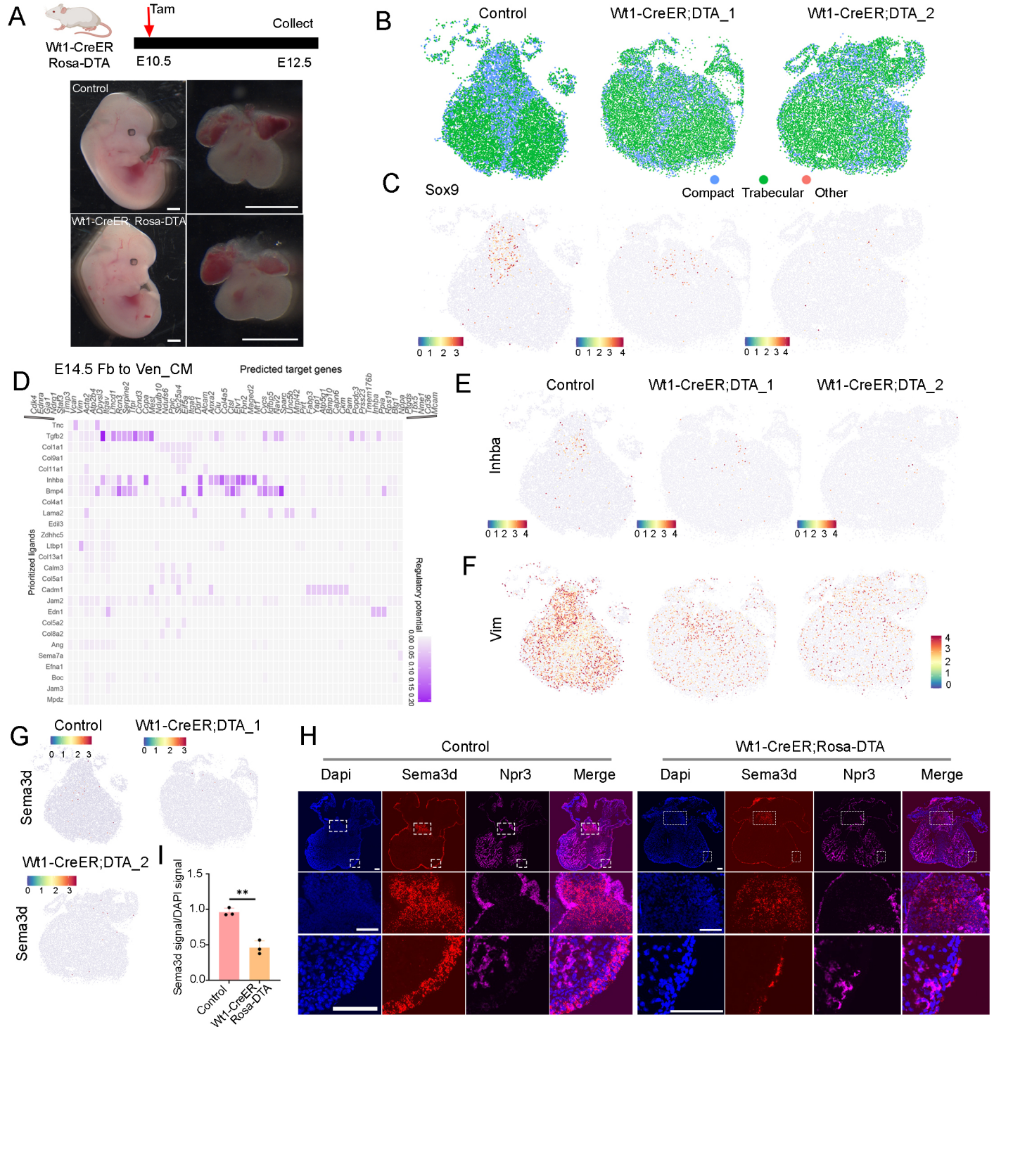
A
Tam
Collect
Wt1-CreER
Rosa-DTA
E10.5
E12.5
Control
Wt1-CreER; Rosa-DTA
B
Control
Wt1-CreER;DTA_1
Wt1-CreER;DTA_2
C
Sox9
Compact
Trabecular
Other
D
E14.5 Fb to Ven_CM
Predicted target genes
Prioritized ligands
Regulatory potential
E
Inhba
F
Vim
G
Sema3d
H
Dapi
Sema3d
Npr3
Merge
Wt1-CreER;Rosa-DTA
I
Sema3d signal/DAPI signal
**